PERTURBED ANGULAR CORRELATIONS - ^{152}Sm AND ^{152}Gd

PERTURBED ANGULAR CORRELATIONS - ^{152}Sm AND ^{152}Gd

By

MICHAEL BRIAN BYRNES, B.Sc.

A Thesis

Submitted to the Faculty of Graduate Studies

in Partial Fulfilment of the Requirements

for the Degree

Master of Science

McMaster University

June 1971

MASTER OF SCIENCE
(Physics)

McMASTER UNIVERSITY
Hamilton, Ontario

TITLE: Perturbed Angular Correlations - ^{152}Gd and ^{152}Sm.

AUTHOR: Michael Brian Byrnes, B.Sc. (Western University)

SUPERVISOR: Dr. J.A. Cameron

NUMBER OF PAGES: vi, 59

SCOPE AND CONTENTS:

Using the technique of perturbed angular correlations, the rotation of the 4 + 366 keV ^{152}Sm level and the rotation of the 2 + 344 keV ^{152}Gd level was observed. These nuclei were the daughter nuclei of ^{152}Eu, present in the europium - gadolinium and europium - holmium alloys which were commercially obtained (europium concentration was about 1% in both alloys). Anomolously low fields were obtained for ^{152}Gd in gadolinium and in the holmium which raised doubts as to the homogeneity of the alloys.

Samples of the alloys were analysed metallurgically. After chemical treatment and microscopic examination the presence of inclusions was detected. Electron microprobe examinations indicated that the inclusions were europium. The metallurgical analysis confirmed the doubts raised by the nuclear experiments showing that the two methods can be employed complementarily for alloy analysis.

ACKNOWLEDGEMENTS

I wish to take this opportunity to express my appreciation to everyone who has been connected with this work. In particular I would like to thank;

Dr. J.A. Cameron for initiating the project and providing ideas and helpful suggestions;

Dr. W.V. Prestwich and Dr. C.V. Stager for their consultation during the writing of this thesis;

Dr. M.B. Ives for his aid in and initiation of the metallurgical analysis of the alloys;

D.B. Kenyon who designed and built the automated data collection system;

My wife, Elizabeth, who always offered encouragement and love;

My mother who doubled as cryptographer and typist;

Department of Veterans Affairs, Province of Ontario and McMaster Physics department for their financial assistance.

This work was supported by grants to the group by the National Research Council and the Alfred P. Sloan Foundation.

TABLE OF CONTENTS

LIST OF FIGURES

CHAPTER I

INTRODUCTION

The study of perturbations in angular correlations has proven to be a useful tool in studying various aspects of nuclear properties and the nuclear environment. A directional correlation can be perturbed by the interaction between the nucleus and its environment during the time interval between the formation and decay of the intermediate states of a nuclear gamma ray cascade. The nuclear magnetic and electric moments interact with the local-magnetic field and the electric field gradient.

The technique of perturbed angular correlations has had its most frequent application in determining the magnetic moments of excited nuclear states. Recently the method has found application as a probe of the nuclear environment. In particular this may take the form of a study of ferromagnetic properties of the host or studies of electric field gradients or other properties which influence the angular correlation.

Six of the rare earth metals; gadolinium, terbium, dysprosium, holmium, erbium and thulium; exhibit ferromagnetic properties at low temperatures. The internal fields at the nuclei in ferromagnetic rare earth metals range from 0.3 to 9 megagauss. These values are within the range appropriate for utilizing the technique of perturbed angular correlations.

The internal magnetic field at the nucleus in rare earths is believed to be mainly due to the 4f electrons. Thus any variation of magnetic field on a nucleus with different neighbouring rare earths, could yield information about the basic interaction in rare earth magnetism. A systematic study was initiated into the variation of internal magnetic field with host for a given impurity nucleus.

In the course of the investigation the emphasis changed to making use of perturbed angular correlations techniques as a probe of the effective magnetic field on a rare earth nucleus in an "alloy" to determine if the alloy is truly homogeneous. These experiments were done in 1% alloys of europium in gadolinium and holmium. The daughter nuclei of ^{152}Eu; ^{152}Gd and ^{152}Sm; were used as the "probes". By applying the technique of perturbed angular correlations to the gamma ray cascades a value for the average magnetic field acting on the nuclei can be determined. As the magnetic field varies with the surroundings of the nucleus observed, then the average magnetic field can yield an estimate of the amount of europium in a homogeneous solid solution with gadolinium and holmium.

CHAPTER II

GENERAL THEORY

Gamma rays belonging to the same cascade of a given nucleus exhibit a directional correlation. This correlation can be perturbed by the effect of the interactions between the nucleus and its environment, while the nucleus is in the excited intermediate level of the cascade. These interactions between a nucleus and its environment cause the nucleus to precess, analogous to the case of a force acting upon a gyroscope, and in the experiment the precession of the nucleus while in the intermediate level is observed indirectly. In this chapter a non-rigorous development of directional correlations and perturbed angular correlations will be followed by a description of rare earth magnetism.

1. Perturbed Angular Correlations

The discussion of angular correlation theory and perturbed angular correlation theory below, follows the theory as developed by R.M. Steffen and H. Frauenfelder (1965).

In general the angle between the nuclear spin axis and the direction of emission of a particle by a radioactive nucleus determines the probability of that emission. As the nuclei usually have a random orientation the angular distribution becomes isotropic. However, a non-random

array of nuclei can be achieved by a strong magnetic field, electric field gradient or choosing nuclei whose spins lie in a preferred direction. The last case can be achieved if a nucleus decays by successive emission of two radiations R_1 and R_2. The observation of R_1 in a fixed direction selects a non-random subset of possible nuclear orientations from the random array. Thus R_2 may have a definite directional correlation with respect to R_1.

Consider the emission of gamma ray γ_1 between pure nuclear states I_i, m_i and I,m where γ_1 is characterized by the angular momentum quantum number L_1 and magnetic quantum member M_1. In order to conserve angular momentum $\bar{I}_1 = \bar{I} + \bar{L}_1$ and $m_i = m + M_1$.

Each component $m_i \rightarrow m$ between specific magnetic substates possess a characteristic angular distribution $F_M^L(\phi)$ with respect to the quantization axis, independent of I_i and I. This directional distribution is found by calculating the energy flow (Poynting vector) as a function of angle for the multipole radiations involved. As the various M components of the gamma rays are usually not resolved one sees the distribution $F_{L_1}(\phi)$, where $F_L(\phi) \propto \sum_{m_i m} P(m_i)\, G(m_i m)\, F_{L_1}^{M_1}(\phi)$ $P(m_i)$ is the relative population of sublevel m_i and $G(m_i m)$ is the probability of the transition $m_i \rightarrow m$.

$$\text{i.e. } G(m_i,m) \propto \langle I m L_1 M_1 | I_i m_1 \rangle^2.$$

As the distribution $W(\theta)$ for the $\gamma_1 - \gamma_2$ cascade must be independent of the choice of the z direction, this

allows a simplification by choosing $\bar{k}_1$, the direction of propagation of γ_1, parallel to the z direction. A photon can only have an angular momentum component of $\pm$ h along its direction of motion when it propagates in a definite direction.

Thus if one assumes an equal population of levels and γ_2 $(L_2 M_2)$ joins pure nuclear states Im and $I_f m_f$ then

$$W(\theta) \propto \sum_{m_1 m m_f} \langle I m L_1 \pm 1 | I_i m_i \rangle^2 F_{L_1}^{\pm 1}(0) \langle I_f m_f L_2 M_2 | I m \rangle^2 F_{L_2}^{M_2}(\theta).$$

This summation is incoherent as the result of the selection rule $M = m_i - m = \pm 1$.

The above development suffers from three shortcomings: it is not rigorous, contains tedious sums over unobserved quantum numbers and applies only to the directional correlation of two pure gamma rays emitted by free and unpolarized nuclei. In typical cases the initial radiation can be of mixed multipole character and only the statistical population of the intermediate and final states have been determined. Also the nuclei are not free and unpolarized but are subject to environmental effects which introduce perturbations. These perturbations can change the relative populations of the substates of the intermediate level between the time of decay into and out of the intermediate level. This statistical ensemble of nuclei can be handled by employing the density matrix formalism.

The eigenfunctions of the radiation emitted in a direction $\bar{k}$ with a spin $\bar{\sigma}$ can be denoted as $\langle \bar{k} \sigma | LM \Pi \rangle$ corresponding to the eigenvalues L, M, Π of the operators

for angular momentum, the z component of angular momentum and parity respectively.

Making use of the density distribution $\varrho(\bar{k}_1)$, which describes the end product of the first transition, as well as, representing the rearrangement of the intermediate state while exposed to an extranuclear perturbation, one obtains for the transition $I_i \rightarrow I$

$$\langle m | \varrho(\bar{k}_1) | m' \rangle = S_1 \sum'_{m_i m_i'} \langle m | \mathcal{H}_1 | m_i \rangle \langle m_i | \varrho_1 | m_i' \rangle \langle m' | \mathcal{H}_1 | m_i' \rangle^* .$$

$\varrho(\bar{k}_1)$ is the density distribution of the intermediate level, S_1 represents the sum over unobserved radiation properties, and $\mathcal{H}_1$ is the operator inducing the transition.

Thus

$$\langle m_f | \varrho(\bar{k}_1, \bar{k}_2) | m_f' \rangle = S_1 S_2 \sum'_{\substack{mm' \\ m_i m_i'}} \langle m_f | \mathcal{H}_2 | m \rangle \langle m | \mathcal{H}_1 | m_i \rangle \times \langle m_i | \varrho_i | m_i' \rangle \langle m' | \mathcal{H}_1 | m_i' \rangle^* \times \langle m_f | \mathcal{H}_2 | m' \rangle^* .$$

If the states are selected so that the density matrix is diagonal then

$$\langle m' | \varrho | m \rangle = c_m \delta_{mm'} .$$

Thus

$$W(\bar{k}_1, \bar{k}_2) = S_1 S_2 \sum'_{m_f m m' m_f'} \langle m_f | \mathcal{H}_2 | m \rangle \langle m | \mathcal{H}_1 | m_1 \rangle \times \langle m' | \mathcal{H}_1 | m'_i \rangle^* \langle m_f | \mathcal{H}_2 | m' \rangle^* \quad (1)$$

but

$$\langle m | \mathcal{H} | m_i \rangle \equiv \langle I m k \sigma | \mathcal{H} | I_i m_i \rangle$$

and since $\mathcal{H}$, the transition operator is invariant under rotations then

$$\langle I_f m_f L M \pi | \mathcal{H} | I_i m_i \rangle = \langle I_f m_f L M | I_i m_i \rangle \langle I_f \| L \pi \| I_i \rangle$$

where $\langle I_f \| L \pi \| I_i \rangle$ is the reduced transition matrix and

$$\langle m | \mathcal{H} | m_i \rangle = \sum_{LM\pi} \langle k \sigma | LM \pi \rangle \langle I_f m_f L M | I_i m_i \rangle \langle I_f \| L \pi \| I_i \rangle$$

$$\langle k \sigma | LM \pi \rangle = \sum_{\mu} \langle o \sigma | L \mu \pi \rangle D^{L}_{M\mu}(\bar{z} \to \bar{k})$$

then $\langle m | \mathcal{H} | m_i \rangle = \sum_{L \pi \mu} (-1)^{-I_f + L - m_i} \begin{pmatrix} I_f & L & I_i \\ m & M & -m_i \end{pmatrix} \langle o \sigma | L \mu \pi \rangle \times$

$$\times \langle I_f \| L \pi \| I_i \rangle D^{L*}_{M\mu}(\bar{z} \to \bar{k})$$

where $D^{L}_{M\mu}(\bar{z} \to \bar{k})$ is the rotation matrix describing the rotation that carries the arbitrary quantization system $\bar{z}$ over into the coordinate system of the radiation and $\begin{pmatrix} I_f & L & I_i \\ m & M & -m_i \end{pmatrix}$ is the Wigner 3-j symbol.

using

$$C_{k\tau}(LL') = S \sum_{\mu\mu'} (-1)^{L-u} (2k+1) \begin{pmatrix} L & L' & k \\ \mu & -\mu' & -\tau \end{pmatrix} \times$$

$$\times \langle o \sigma | L \mu \pi \rangle^{*} \langle o \sigma' | L' \mu' \pi' \rangle$$

where $\begin{pmatrix} L & L' & k \\ \mu & -\mu & -\tau \end{pmatrix}$ are Wigner 3-j symbols

then $W(\bar{k}_1, \bar{k}_2) = (-1)^{2I - I_i - I_f} \sum_{k} \sum_{L_1 L_1' L_2 L_2'} \sum_{\tau_1 \tau_2} (-1)^{k - L_1' - L_2'} \begin{Bmatrix} I & I & k \\ L_1' & L_1 & I_i \end{Bmatrix} \times$

$$\times \begin{Bmatrix} I & I & k \\ L_2 & L_2' & I_f \end{Bmatrix} \langle I_f \| L_2 \pi_2 \| I \rangle \times$$

$$\times \langle I_f \| L_2' \pi_2' \| I \rangle^{*} \langle I \| L_1 \pi_1 \| I_i \rangle \times$$

$$x \langle I \| L_1' \pi_1' \| I_i \rangle^* \times C_k \tau_1 (L_1' L_1) \times$$

$$x C_k^* \tau_2 (L_2 L_2') D^k \tau_2 \tau_1 (\bar{k}_2 \rightarrow \bar{k}_1)$$

where $\begin{Bmatrix} I & I & k \\ L_1 & L_1' & I_i \end{Bmatrix}$ is a Wigner 6-j symbol .

The rotation $\bar{k}_2 \rightarrow \bar{k}_1$, carries the coordinate system of the second radiation into that of the first.

As the correlation function must be independent of the angle of rotation about the directions of propogation $\tau_1 = \tau_2 = 0$. Thus the representations D^k become Legendre polynomials. Therefore

$$W(\bar{k}_1, \bar{k}_2) = W(\theta) = \sum_{k \text{ even}} A'_{kk} P_k(\cos\theta)$$

$$A'_{kk} = A'_k(L_1 L_1' I_i I) \, A'_k(L_2 L_2' I_f I)$$

where

$$A'_k(L_1 L_1' I_i I) = \sum_{L_1 L_1'} (-1)^L C_{ko}(L_1 L_1') \begin{Bmatrix} I & I & k \\ L_1 & L_1' & I_i \end{Bmatrix} x$$

$$x \langle I \| L_1 \pi_1 \| I_i \rangle \langle I \| L_1' \pi_1' \| I_i \rangle^*$$

and

$$A'_k(L_2 L_2' I_f I) = \sum_{L_2 L_2'} (-1)^{L_2} C^*_{ko}(L_2 L_2') \begin{Bmatrix} I & I & k \\ L_2 & L_2' & I_f \end{Bmatrix} x$$

$$x \langle I \| L_2 \pi_2 \| I_f \rangle^* \langle I \| L_2' \pi_2' \| I_f \rangle .$$

A perturbation, described by the Hamiltonian K, is now assumed to act from the time of the first emission, γ_1, until the second emission, γ_2. The form of $W(\bar{k}_1, \bar{k}_2)$ given in equation 1 is employed. The interaction K results in states $|m_a\rangle$ evolving to different states $|m_b\rangle$. The perturbed correla-

tion can then be expressed as

$$W(\bar{k}_1\bar{k}_2t) = \sum_{\substack{m_i m_f \\ m_a m_a'}} \langle m_f | \mathcal{H}_2 \Lambda(t) | m_a \rangle \langle m_a | \mathcal{H}_1 | m \rangle \times \langle m_f | \mathcal{H}_2 \Lambda(t) | m_a' \rangle^* \langle m_a' | \mathcal{H}_1 | m \rangle^*$$

where $\Lambda(t)$ is the evolution operator and

$$\Lambda(t)|m_a\rangle = \sum_{m_b} |m_b\rangle \langle m_b | \Lambda(t) | m_a \rangle$$

similarly for $\Lambda(t)|m_a'\rangle$.

As $\Lambda(t)$ satisfies the Schrodenger Equation

$$\Lambda(t) = \exp\left(-\frac{i}{\hbar} \int_0^t K(t')\, dt' \right)$$

for a time dependent K.

$$\Lambda(t) = \exp -\frac{i}{\hbar} K t$$

if K is time independent.

Therefore

$$W(\bar{k}_1\bar{k}_2t) = \sum_{\substack{m_a m_a' \\ m_b m_b'}} \langle m_a | \rho(\bar{k}_1) | m_a' \rangle \langle m_b' | \rho(\bar{k}_2) | m_b \rangle \times \langle m_b | \Lambda(t) | m_a \rangle \langle m_b' | \Lambda(t) | m_a' \rangle^* .$$

Employing definitions of A_k, expressions for the density matrix and spherical harmonics.

$$W(\bar{k}_1\bar{k}_2t) = \sum_{\substack{k_1 k_2 \\ N_1 N_2}} A_{k_1}(1)\, A_{k_2}(2)\, G_{k_1 k_2}^{N_1 N_2}(t) \left[(2k_1+1)(2k_2+1)\right]^{-\frac{1}{2}} \times Y_{k_1}^{N_1}(\theta_1\phi_1)\, Y_{k_2}^{N_2}(\theta_2\phi_2)$$

See Figure II-1 for angle definitions

where

$$G_{k_1 k_2}^{N_1 N_2}(t) = \sum_{m_a m_b} (-)^{2I + m_a + m_b} \left[(2k_1+1)(2k_2+1)\right]^{\frac{1}{2}} \times$$

Fig. II-1. Angular coordinates of the propogation direction $\overline{k}_1$ and $\overline{k}_2$. Z corresponds to the direction of the external field.

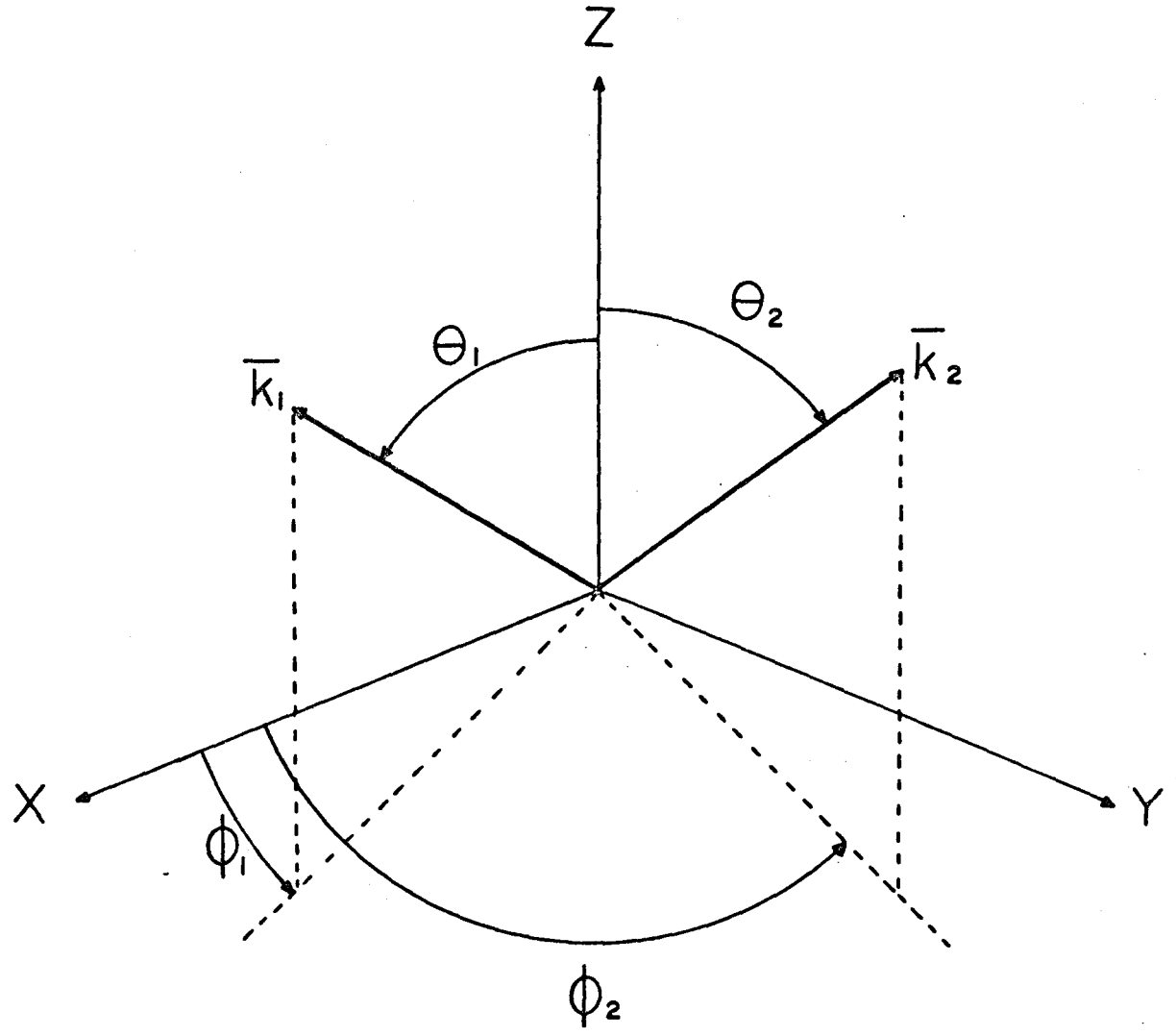
Z
θ_2
θ_1
$\bar{k}_1$
$\bar{k}_2$
X
Y
ϕ_1
ϕ_2

$$x \begin{pmatrix} I & I & k_1 \\ m_a' & -m_a & N_1 \end{pmatrix} \begin{pmatrix} I & I & k_2 \\ m_b' & -m_b & N_2 \end{pmatrix} x$$

$$x \langle m_b | \Lambda(t) | m_a \rangle \langle m_b' | \Lambda(t) | m_a' \rangle^* .$$

In the case of static interactions

$$\langle m_b | \Lambda(t) | m_a \rangle = \sum_n \langle n | m_b \rangle^* \left[\exp -\left(\frac{i}{\hbar} \right) E_n t \right] \langle n | m_a \rangle .$$

If the symmetry axis of the interaction is chosen parallel to z

$$\langle m_b | \Lambda(t) | m_a \rangle = e^{-(i/\hbar) E_m t} \delta_{m m_a} \delta_{m m_b} .$$

There is intrinsically a finite time resolution of coincidence circuits which are employed in cascade angular correlation measurements. Only the perturbation factos $G_{k_1 k_2}^{N_1 N_2}(t)$ depend on the time t, therefore the time integrated perturbation coefficients can be defined as

$$\overline{G_{k_1 k_2}^{N_1 N_2}}(T) = \frac{\int_0^\infty f(t - T) \, G_{k_1 k_2}^{N_1 N_2}(t) \, e^{-t/\tau} \, dt}{\int_0^\infty f(t - T) \, e^{-t/\tau} \, dt}$$

$f(t - T)$ is the time response function of the system. t is time of acceptance of the second radiation, and T is the delay of that channel. τ is the mean life of the intermediate state.

If the resolving time of the circuit is much longer than τ

$$\overline{G^{N_1N_2}_{k_1k_2}}(T) = \frac{1}{\tau} \int_0^\infty G^{N_1N_2}_{k_1k_2}(t)\, e^{-t/\tau}\, dt \quad .$$

The Hamiltonian describing the interaction between the nuclear magnetic moment u of the intermediate state and the magnetic field H which is parallel to the axis is $K_H = \vec{\mu}\cdot\vec{H} = -\mu_z H$. Thus the energy eigenvalues are $E_m = \mu \frac{Hm}{I}$

$$= m\hbar\omega$$

where ω is the Lamor frequency.

$$\omega = \left(\frac{E_{m+1} - E_m}{\hbar}\right) = \frac{g\mu_n H}{\hbar} \quad .$$

This interaction results in a precession of the nucleus about the field direction at a frequency ω which effectively rotates the directional correlation pattern by ωt, where t is the time elapsed between the emission of the first and the second gamma ray. Then the pattern is given by the time dependent form.

$$W(\theta,H,t) = \sum_k A_{kk} P_k (\cos\theta - \omega t)$$

In the case of an interaction between an electrostatic field gradient and the electrical quadrupole moment

$$V_q = \sum_q \frac{4}{5}\pi (-1)^q T_q^{(2)} V_q^{(2)} \quad .$$

Where $T_q^{(2)}$ and $V_q^{(2)}$ are the tensor operators of the nuclear quadrupole moment and the classical external field gradient.

The interaction matrix is:

$$\langle I_m | K_q | I_m' \rangle .$$

The conventional definition of the quadrupole moment is:

$$eQ = 4 \sqrt{\frac{1}{5}} \langle II | T_o^{(2)} | II \rangle .$$

If the field is axially symmetric the interaction Hamiltonian becomes

$$K_q = \sqrt{\frac{1}{5}} \pi T_o^{(2)} V_{zz} .$$

Then the elements of the interaction matrix are diagonal. Therefore the quadrupole interaction matrix element can be shown to be

$$\langle I_m | K_q | I_m \rangle = E_m = \frac{3m^2 - I(I+1)}{4I(2I-1)} e Q V_{zz} .$$

The quadrupole frequency is $\omega_q = - \frac{e Q V_{zz}}{4I(2I-1)\hbar}$.

Since the energy eigenvalues E_m depend upon m^2 they are doubly degenerate, unless m = o, so that the quadrupole rotations are insensitive to the direction of the magnetic field. Thus when a magnetic field is the main perturbing interaction, the quadrupole effects reduce the anisotropy of the angular distribution. This is true in the cases discussed below. As $\omega_E >> \omega_q$, this leads to a smearing out of the effects of the quadrupole interaction and the electrical and magnetic interactions can then be treated individually.

2. Measurement of the Rotation

For analytical convenience the expression

$$W(\theta,H,t) = \sum_n B_{2n} \cos 2n(\theta - \omega t)$$

will be used, which is equivalent to the form of $W(\theta,H,t)$ developed in an above section.

In the actual experiments the resolving time of the apparatus was much longer than the mean life τ of the intermediate state so that the time integrated correlation was observed.

Therefore

$$W(\theta,H,\infty) = \frac{1}{\tau} \int_0^\infty e^{-t/\tau} W(\theta,H,t)\, dt \ .$$

Hereafter $W(\theta,H) \equiv W(\theta,H,\infty)$

The above equation for $W(\theta,H)$ may be readily integrated to give

$$W(\theta,H) = \sum_n \frac{B_{2n}}{1+(2n\omega\tau)^2} (\cos 2n\theta + 2n\omega\tau \sin 2\theta) .$$

The angular correlation pattern is obtained with no magnetic field present. An angle θ' is then chosen so that $\frac{dW}{d\theta}$ is near a maximum and also where it is convenient to measure the coincidence rates. The coincidence rates are then measured at the angle θ' in a magnetic field with the direction of the field successively "up" and "down". The experimentally determined quantity is $\frac{R}{2}$

where

$$\frac{R}{2} = \frac{W(\theta',H) - W(\theta', -H)}{W(\theta',H) + W(\theta', -H)}$$

$$= \frac{\sum_n \frac{B_{2n}}{1+(2n\omega\tau)^2} 2n\omega\tau \sin 2n\theta'}{\sum_n \frac{B_{2n}}{1+(2n\omega\tau)^2} \cos 2n\theta'}$$

If $\omega\tau \ll 1$ then

$$\frac{R}{2} = -\left[\frac{1}{W(\theta)}\frac{dW(\theta)}{d\theta}\right]_{\theta}, \quad \frac{g\mu_N H}{\hbar} \qquad . \quad (2)$$

Thus the rotation depends on the g-value of the intermediate state, the field H acting upon the nucleus and the mean life τ of the intermediate level.

3. Effective Field at the Nucleus

The effective magnetic field acting at a nucleus may be considered to consist of a number of terms

$$\bar{H}_{eff} = \bar{H}_{mac} + \bar{H}_{hyp}$$

where $\bar{H}_{mac}$ is the macroscopic field acting throughout the crystal and $\bar{H}_{hyp}$ is the field acting on the nucleus through the hyperfine interaction.

$\bar{H}_{mac}$ consists of several terms. It includes the external magnetic field, the Lorentz field and the demagnetizing field. $\bar{H}_{mac}$ is usually much less than the measured effective field.

The $\bar{H}_{hyp}$ is due to the Fermi contact interaction and the interaction of the nucleus with the magnetic dipole moments of the electrons on the same atom. For the Fermi contact interaction if no unpaired s-electrons exist but the outer s-electrons possess a net spin, then the core electrons can be polarized by the spin of the outer electrons to produce a net spin density at the nucleus. The remainder of $\bar{H}_{hyp}$ consists of the dipole - dipole interaction between

nuclear and electron spins, the interaction between the nucleus and the unquenched part of the orbital moment; and the cross terms between the dipole - dipole interadtion and spin-orbit coupling.

In the rare earth metals the dominant effects are caused by the orbital angular momentum of the unfilled 4f shell, and to a lesser extent, the spin exchange polarization of core and conduction electrons. In most rare earths the orbital angular momentum is almost completely unquenched and produces a field of several megagauss. Exceptions to this are gadolinium and europium, which have a half filled 4f electron shell and the fields are smaller, 340 and 267 kilogauss respectively.

Only the component of the rotation of the nucleus in the plane of the detectors is observed. Since the detectors are in a plane perpendicular to the applied magnetic field in these experiments the observed rotation is perpendicular to the external field. Therefore, the average relative orientation of the nuclear magnetic moments with respect to the external field is observed via the sign and size of H_{obs}. The observed magnetic field (i.e. H in equation 2) is given by $H_{obs} = H_{eff} \cos \theta$ where θ represents the average angle between the nuclear magnetic moments and the external field director.

4. Rare Earth Ferromagnetism

In the following paragraphs the properties of the

rare earth metals that are relevant for the experiments will be discussed. A brief summary of the crystallography and magnetic properties will be presented first. Next a discussion of the origins and size of the magnetic field at the nucleus will be presented. In these experiments the anisotropy energy plays a large role. The effects of the anisotropy energy on the rare earth metals will also be discussed.

In general the rare earth elements are characterized by one to fourteen electrons in the 4f shell, while the valence electrons are usually the three electrons in the 5d and 6s orbitals. The rare earth metals usually crystallise into a hexagonal close-packed structure with ratio of c axis to a axis in the range 1.57 to 1.59. Notable exceptions are europium and ytterbium which have body centred cubic structure and face centred cubic structures respectively.

Many of the rare earth metals are ferromagnetic below some temperature T_c and are antiferromagnetic above T_c. Only gadolinium has no antiferromagnetic phase with the Curie temperature for gadolinium being 290°K. The rest of the rare earths have a deformed screw structure. The anisotropy energy for the rare earth metals arises mainly from the electrostatic interaction between the multipole moments possessed by the 4f electrons and the crystalline field produced by the surrounding charge distributions. This anisotropy energy produces the transition from the antiferromagnetic phase to a simple ferromagnet with moments in the

hexagonal plane.

The form of the anisotropy energy appropriate for hexagonal symmetry is given by

$$\mathcal{A} = D\,P_2(\cos\theta) + E\,P_4(\cos\theta) + F\,P_6(\cos\theta) + G\sin^6\theta\cos 6\phi$$

where $P_n(\cos\theta)$ is the Legendre polynomial of degree n and θ and ϕ are the polar and azmithual angles of the magnetic moment J. D,E,F and G are anisotropy constants which determine the preferred direction of the ordered moment with respect to the crystal axes.

In the rare earth metals the magnetization is thought to be mainly due to the 4f electrons. However, unlike the case of the 3d transition elements the 4f wave functions are localized in the vicinity of the nucleus. The 4f wavefunctions of neighbouring atoms have negligible overlap, thus it would be presumed that an indirect interaction between 4f electrons would be dominant and hence the cause of magnetic ordering.

It is believed that the indirect exchange interaction between 4f electrons via the conduction electrons is the Rudderman-Kittel-Kasuya-Yosida Interaction (Koehler 1965). It is long range and oscillatory in space. The interaction between the 4f electrons on different rare earth ions are believed to interact by the double scattering of an electron between an occupied state in the Fermi surface into any available state. The spin on one atom may be regarded as setting

up a spin polarization in the conduction electrons. Because the Fermi distribution restricts the wave vector of the electrons which carry the polarization, this polarization tends to have an oscillatory component. The polarization couples to the spins of other atoms to produce an effective exchange with a long range nature.

Some of the rare earths possess an easy and hard direction for magnetization. Because of the large anisotropy energy it is virtually impossible to magnetically saturate the sample along the c axis with the external fields employed. Thus it must be assumed that H_{eff} is perpendicular to $\bar{c}$ and that the magnetization seen will be due to the projection of the moments on the directions of the applied field. Then integrating over all orientations of the basal plane and the possible directions of easy magnetization in the basal plane we obtain $M_{metal} = \frac{3}{4} M$ easy direction.

CHAPTER III

EXPERIMENTAL APPARATUS

In the following sections the equipment employed in the experiments is briefly outlined. Mentioned first are the cryostats and magnets along with the necessary magnetic shielding. Next the functional details of the data collection and storage system, as well as, how the experiments are automatically controlled, are given. In the final section the angular correlation table is described. The basic apparatus essential to the experiment is a magnet, scintillation detectors coupled to photomultiplier tubes, a system for pulse analysis, and a means of determining the angle between detectors.

1. Cryostats and Magnets

A superconducting magnet is suspended inside a pair of glass dewars by thin wall stainless steel tubes which gain rigidity from brass plates perpendicular to their length as shown in Figure III-1. Both dewars are silvered on their inner vacuum jacket surfaces to minimize radiation heating. The outer dewar is filled with liquid nitrogen while the inner dewar holds about three litres of liquid helium.

The helium part of this system was made leakproof via O-ring seals and hermetically sealed electrical feed-through connectors in order to prevent air from contaminating the helium.

Fig. III-1. Superconducting magnet dewar setup. The helium is returned via the return line to be reliquified.

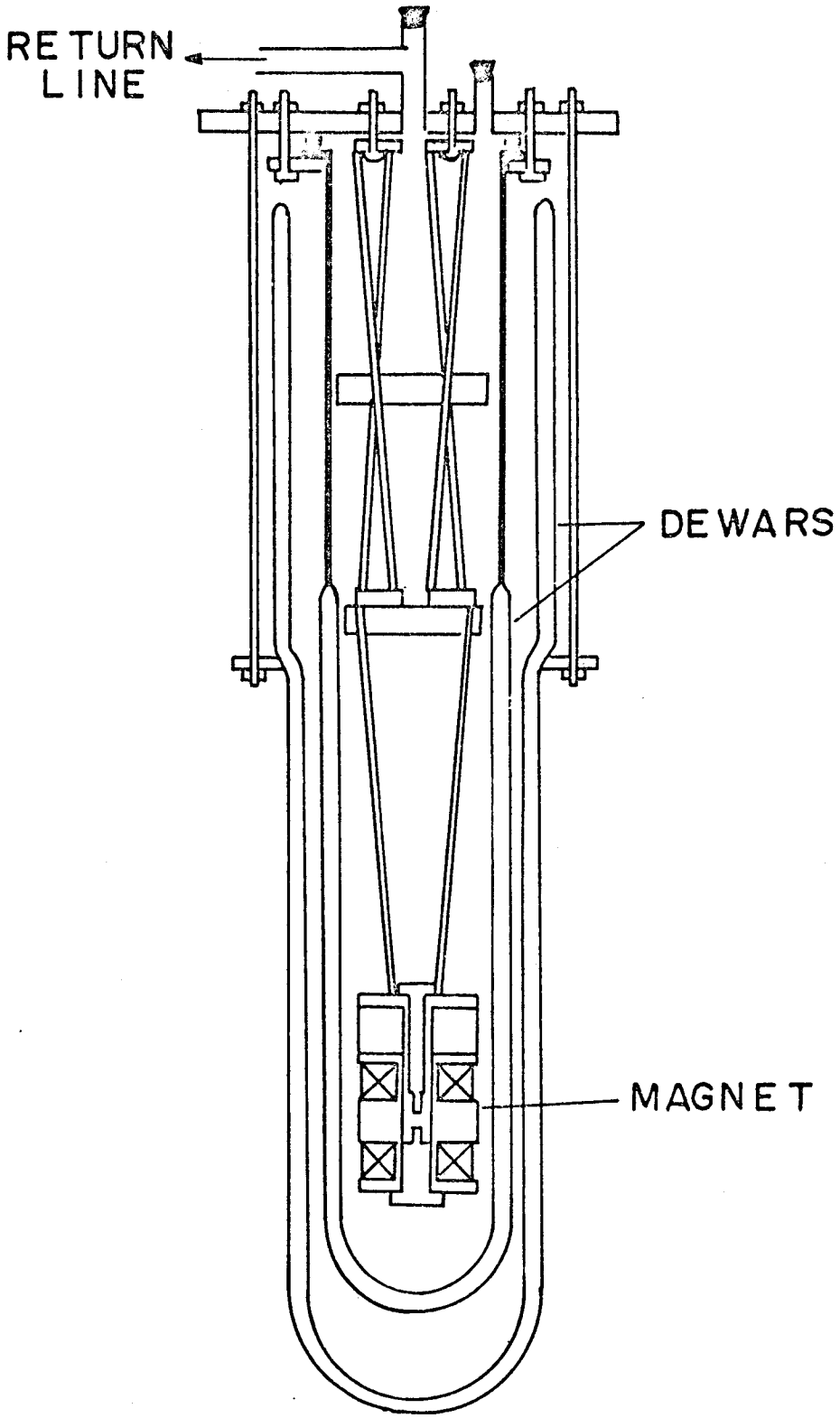
RETURN
LINE
DEWARS
MAGNET

The superconducting magnet was custom made by Oxford Instrument Company Limited. It features a split coil arrangement, with two 30° wedge coil spacers, to permit clear passage of radiation over a large range of angles in the horizontal plane. A maximum field of 16.7 kG. is produced which corresponds to a magnet current of 19 amps. The magnet is protected via two diodes in parallel with the magnet. The source is supported in a stainless steel tube which is mounted on the lower aluminum pedestal (see Figure III-1).

The experiments performed at liquid nitrogen temperatures were done in a silvered glass dewar in which the iron magnet was supported on styrofoam. In order to reduce the evaporation rate of liquid nitrogen the dewar had a styrofoam stopper inserted. These experiments were performed on the angular correlation table which is described below.

The iron magnet consists of two coils of 1000 turns each of 20 gauge enamelled copper wire mounted on copper formers. These formers are separated from each other in the mild steel yoke which surrounds the coils to act as a magnetic return path. This yoke has a 1" diameter hole cut out one side and a $1\frac{1}{4}$" high slit of angular length 150° to allow the gamma rays an unobstructed path to the detectors. The pole tips are made of $\frac{1}{4}$" diameter mild steel tapering to 1/8" diameter with a variable gap distance. This magnet produces 2.0 kG. at 1.5 amp with a gap of 0.3 cm.

The stray magnetic field is reduced via a 30 turn

bucking coil carrying a variable fraction of the magnet current.

Both magnets were powered by a Harrison Laboratories 6246A power supply. The supply was operated in a manner to provide constant current through the magnets. In both cases the power supply is operated in a voltage limited constant current mode. For the superconducting magnet experiments a resistor chain is placed in series to provide an adequate voltage drop for stabilization during operation.

2. Magnet Shielding

Since the output from photomultipliers is very sensitive to stray magnetic fields it becomes necessary to employ magnetic shielding for these tubes. Two different types of photomultiplier shields were employed. For the moveable detectors employed in the angular correlation measurements and for the experiments in the presence of a magnetic field at liquid nitrogen temperatures the shielding consisted of a soft iron tube with Conetic AA inner cylinder as shown in Figure III-2, this allowed a smaller angular separation between these moveable detectors at a given source to detector distance than the other magnetic shielding. For the fixed detector in all cases and the moveable detectors for the superconducting magnet experiments the shields were constructed as shown in Figure III-3. Sheets of Netic and Conetic AA, high permeability steel from Perfection Mica Corporation, were formed into three con-

Fig. III-2. Magnetic shielding for the moveable detectors.

Fig. III-3. Magnetic shield for detectors during superconducting magnet experiments.

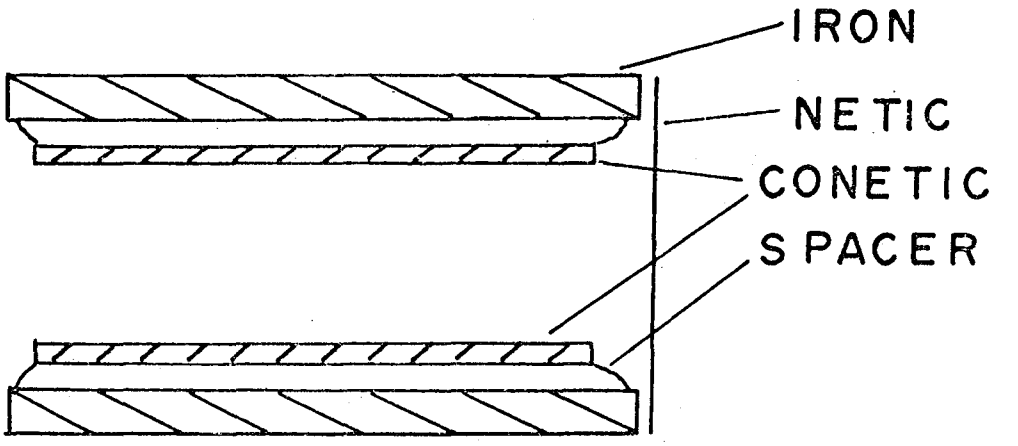
IRON
NETIC
CONETIC
SPACER

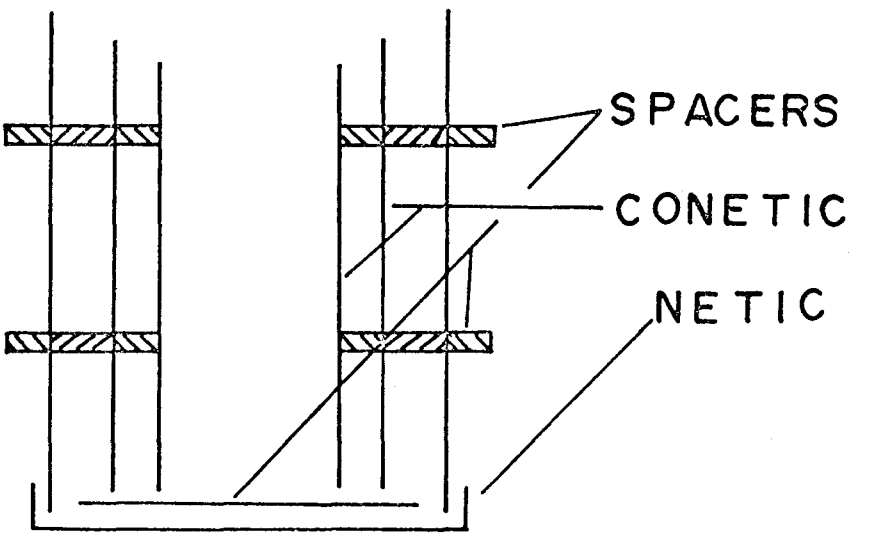
SPACERS
CONETIC
NETIC

centric cylinders separated by aluminum spacers. A Netic cap was fitted over the end of the shield facing the field and placed in contact only with the outer (Netic) cylinder

These latter shields were found to be insufficient shielding for the photomultipliers from the stray magnetic fields due to the super conducting magnet and a subsequent shield was designed surrounding the entire cryostat system with a Netic inner cylinder and a Conetic AA, outer cylinder insulated from each other, which then reduced the magnetic field from about 100 milligauss to about 2 milligauss at the photocathode of the photomultiplier tubes.

3. Data Collecting System

The detectors employed in these experiments are 2" x 2" NaI(Tl) crystals integrally mounted on RCA 6432A photomultipliers. These provide high detection efficiency and a linear response with gamma ray energy. Pulses from the photomultiplier are passed through an Ortec 113 preamplifier and are then amplified and reshaped into bipolar pulses by the Ortec 440A amplifier. These bipolar pulses are then fed into a Canberra 1436 timing single channel analyser (TSCA), where the timing information is derived from the crossover point of the bipolar pulse and the energy information is derived from the pulse peak height. The Canberra 1436 produces two pulses, a "fast" and a "slow" pulse, which are generated, when the energy restrictions established by the window width and baseline controls are met, after the bipolar input signal

crosses the zero voltage level. Both "fast" and "slow" pulses carry timing information and can be delayed. The "fast" pulses, are then fed into a coincidence network as shown in Figure III-4, and the output of this coincidence network is then led to the inputs of the digiplexer. The "slow" pulses from the Canberra 1436's are led directly to the singles input of the digiplexer. As long term stability can be a problem in the experiments Cosmic 101, Spectrastat power supplies are employed as they stabilize on an energy peak in the spectrum and thus can compensate for any overall change in gain due to the photomultiplier, preamplifier and/or amplifier. This effectively eliminates all sources of gain instability prior to the TSCA's.

The data is fed into the programmer (Figure III-5). The programmer via the digiplexer controls whether singles or coincidence counts are stored in the scalers. It can effectively interchange coincidence input 1 with 2 and coincidence input 3 with 4. The interchange of the inputs is arranged to correspond to the reversal of the external magnetic field direction. The coincidence inputs are chosen so that the interchanged inputs are equivalent for the external field in opposite directions.

For example if γ_1 is detected by TSCA's 1A and 2B and γ_2 is detected by TSCA's 1B and 2A where γ_1 and γ_2 are successive gamma rays in the decay cascade, then rotation observed by coincidence rate 1A - 2A with field direc-

Fig. III-4. Block schematic of data collection system excluding programmer.

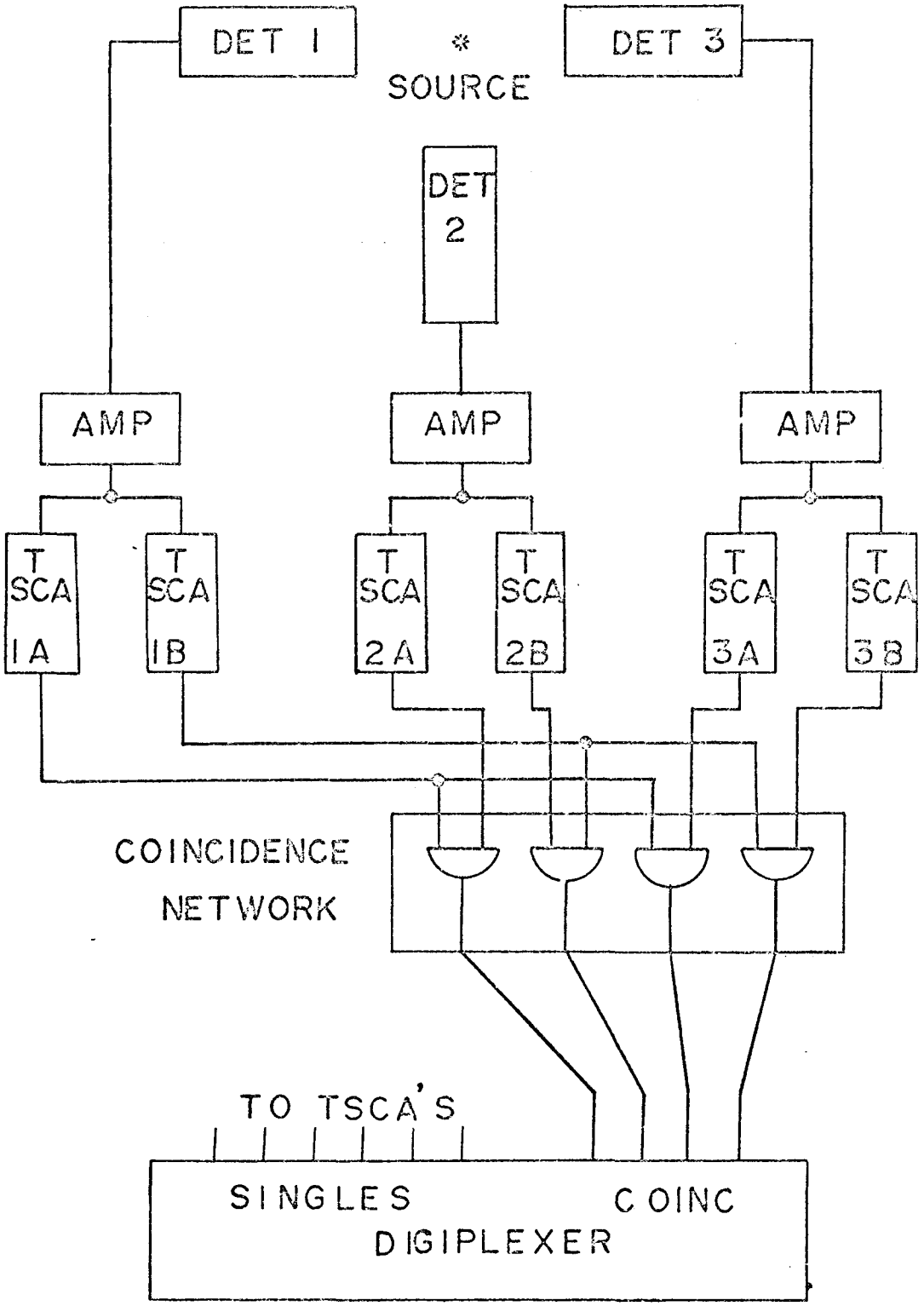
DET 1
SOURCE
DET 3
DET 2
AMP
AMP
AMP
T SCA 1A
T SCA 1B
T SCA 2A
T SCA 2B
T SCA 3A
T SCA 3B
COINCIDENCE NETWORK
TO TSCA'S
SINGLES
COINC
DIGIPLEXER

Fig. III-5. Block schematic of programmer. The digiplexer inputs are the same as those shown in Fig. III-4.

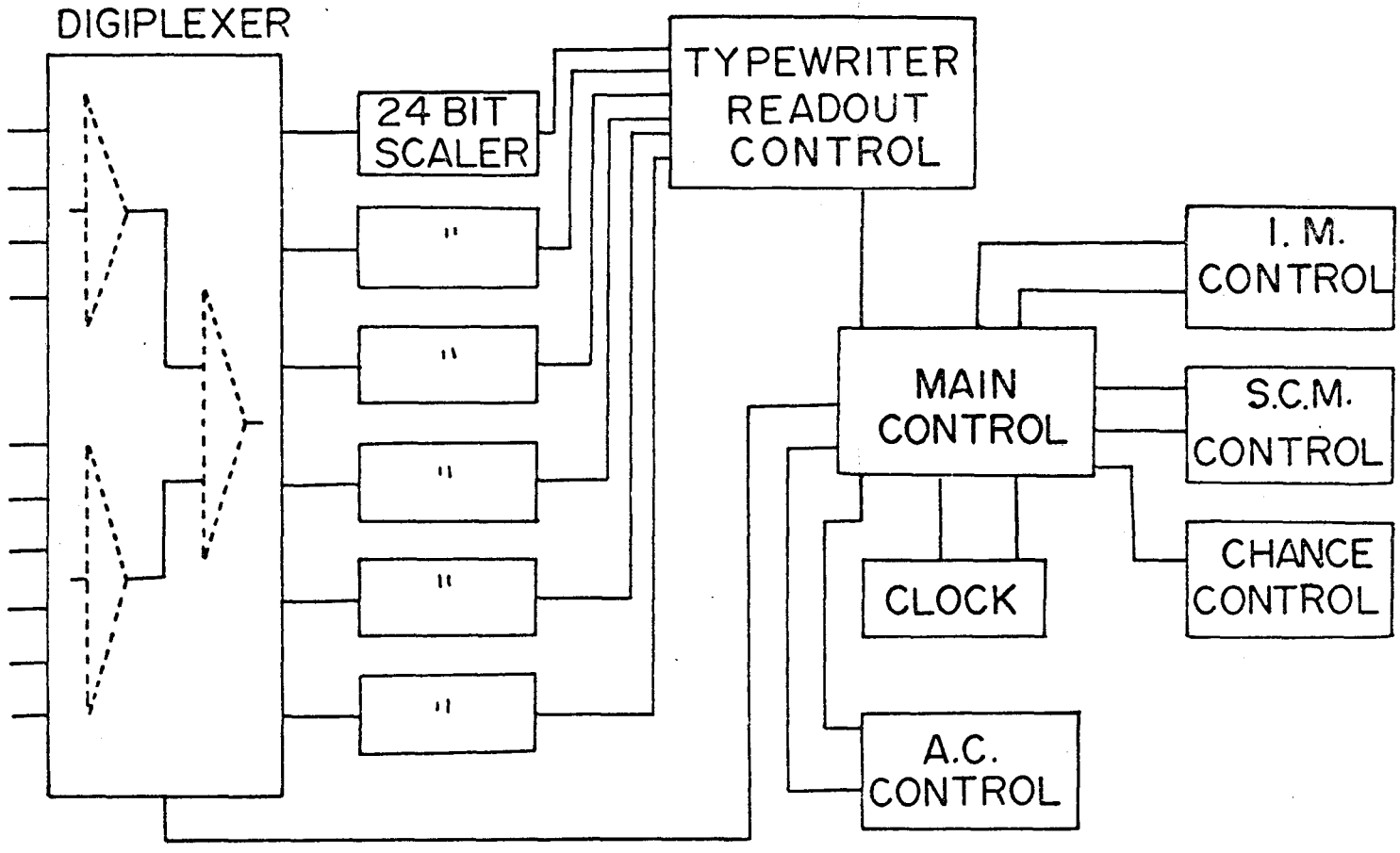
DIGIPLEXER
24 BIT SCALER
"
"
"
"
"
TYPEWRITER READOUT CONTROL
I. M. CONTROL
MAIN CONTROL
S.C.M. CONTROL
CLOCK
CHANCE CONTROL
A.C. CONTROL

tion "up" is the equivalent of the coincidence rate 1B - 2B with the field direction "down". This allows an optimization of the number of detectors employed as well as providing a check on systematic errors.

The main control (see Figure III-4), is basically a timer circuit giving out pulses at times predetermined by the experimenter to control the counting period corresponding to a given field direction, length of storage time between readouts and how often chance coincidence rates are taken. For taking chance rates a delay of 500 n.s. is electronically switched into the "fast" output of TSCA's 1A and 1B. The main control also works as a switching circuit by determining which peripheral control is to be employed; that is the iron magnet control (I.M.) control, superconducting magnet (S.C.M.) control, or the angular correlation (A.C.) control. The former two controls determine the direction of the external magnetic field as well as the switching of the field direction. The A.C. control determines the angle at which the moveable detectors are positioned as well as moving these detectors to other angles.

4. The Angular Correlation Table

The table (Figure III-6 and Figure III-7) has a raised mounting bar for the fixed detector which enables either a NaI(Tl) with magnetic shielding or a Ge(Li) detector with adaptors to be employed. There are two mounting bars which are moveable. One of these is connected to

Fig. III-6. Schematic side view of Angular Correlation table. Detector 2 is shown mounted on the moveable arm and the source is on the moveable stage and pedestal.

Fig. III-7. Schematic top view of the Angular Correlation table. The bar connecting the two moveable arms and the contact holes for the relay rod are shown.

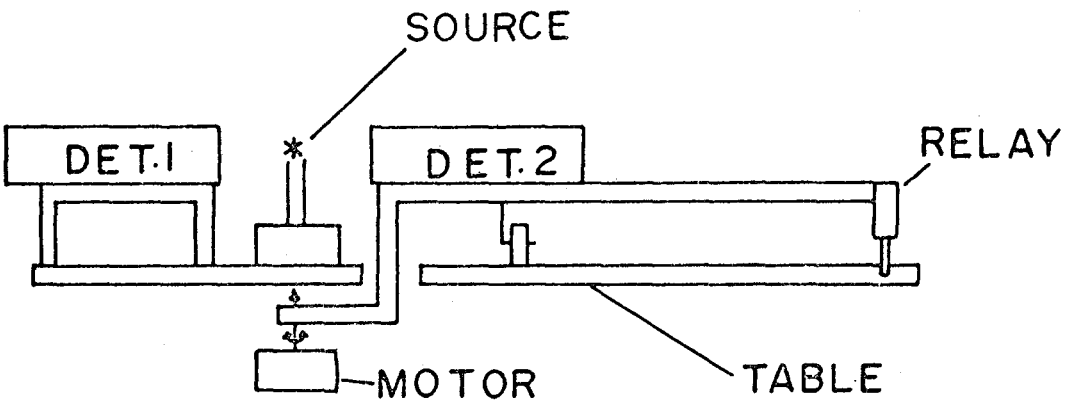
SOURCE
DET.1
DET.2
RELAY
MOTOR
TABLE

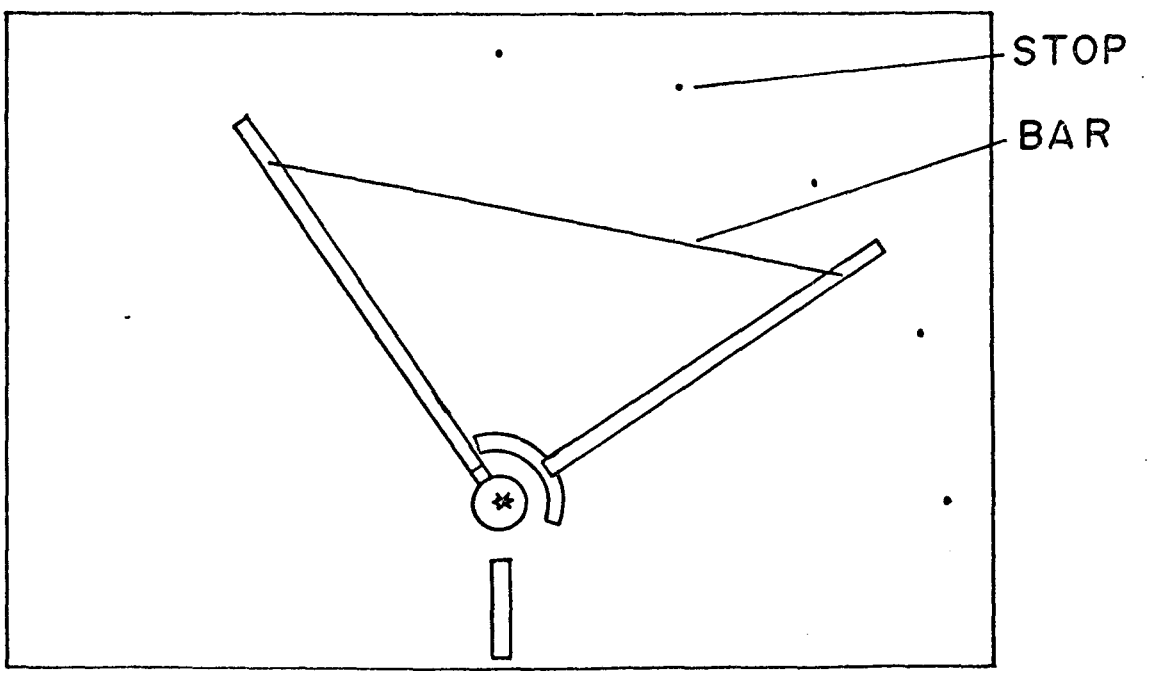
STOP
BAR

a motor which automatically changes the detector angle, the other mounting bar is free moving and its position relative to the motor driven mounting bar can be fixed via a connecting bar which has separations graduated in 10° increments from 40° to 150°. Both of these mobile arms are designed to swing about the centre. The motor driven arm's position can be chosen arbitrarily to within $\frac{1}{2}^{\circ}$. During an angular correlation experiment the arm is motor driven to any one of the 5 holes positioned every $22\frac{1}{2}^{\circ}$ between 90° and 180° with respect to the fixed detector. The arm is stopped by a relay actuated rod dropping into the desired contact hole.

The source is mounted on a thin lucite rod above a moveable stage. This stage is controlled by two micrometer drives operating at 90° to each other and at 45° angles from the longitudinal axis of the fixed detector. This facilitates centring of the source to within a 1% count rate variation over the angles subtended by the moveable detectors.

CHAPTER IV

EXPERIMENTAL

The experiments make use of the time integral method of perturbed angular correlations. In the experiments described below $\omega\tau$ is small so that it is convenient to use:

$$\frac{R}{2} = \frac{W(\theta,H) - W(\theta, -H)}{W(\theta,H) - W(\theta, -H)}$$

as a measure of the rotation.

The experiment consists of first measuring the directional correlation for the desired cascade. This enables the best angle between the detectors to be chosen (usually when $\frac{dW}{d\theta}$ is a maximum). In practice the angular correlation is measured automatically using the equipment described in Chapter III.

At the "best" angle the coincidence rates are measured with the field "up" and the field "down". Thus obtaining R. In practice the external field direction switching is done automatically and the coincidence counts are switched simultaneously from one scaler to another by the programmer described in the above chapter.

The experiments performed were the measurement of the rotation of the 344 keV, 2+ state in ^{152}Gd and the 366 keV, 4+ state in ^{152}Sm, while in the presence of a magnetic field. The decaying nuclei were present in alloys

of europium with gadolinium and holmium. The measurements involving the gadolinium and holmium alloys were performed at 77° K and 4.2° K respectively.

In the sections below the results from the experiments are listed. The method of sample preparation and evalution which include chemical treatment, optical microscope and electron microprobe studies are also described. The results of the perturbed angular correlation experiments and the sample evaluation are discussed.

1. Spectrum and Decay

The gamma spectrum of ^{152}Eu (12.4 years) is somewhat complex and ^{152}Eu decays into two different daughter nuclei - ^{152}Sm by positron decay or electron capture and ^{152}Gd by beta decay. The basic decay scheme for the 12.4 year half life ^{152}Eu is shown in Figure IV-1. The full ^{152}Eu gamma spectrum obtained with a NaI(Tl) detector is shown in Figure IV-2 with the position of the prominent or important peaks labelled by their energy. In the gamma spectrum there is a noticeable asymmetry of the 779 keV peak. This asymmetry is the result of the presence of the 724 keV gamma ray from the decay of ^{154}Eu which has a half life of 16 years. The 724 keV gamma ray has no contribution in the coincidence spectrum as it is not part of the 779 - 344 keV cascade.

The coincidence spectra (Figure IV-3 and Figure IV-4) are obtained by taking the energy spectrum from one detector in coincidence with the output of an energy window

Fig. IV-1. The decay scheme of ^{152}Eu (12 year half life). The intensities of the gamma rays shown are

122 keV	60 %
245	8 %
344	26 %
367	0.5%
411	2 %
444	5 %
779	15 %
869	4 %
965	16 %
1006	1 %
1116	13 %
1213	1 %
1249	0.5%
1298	1.7%
1408	22 %
1455	0.4%

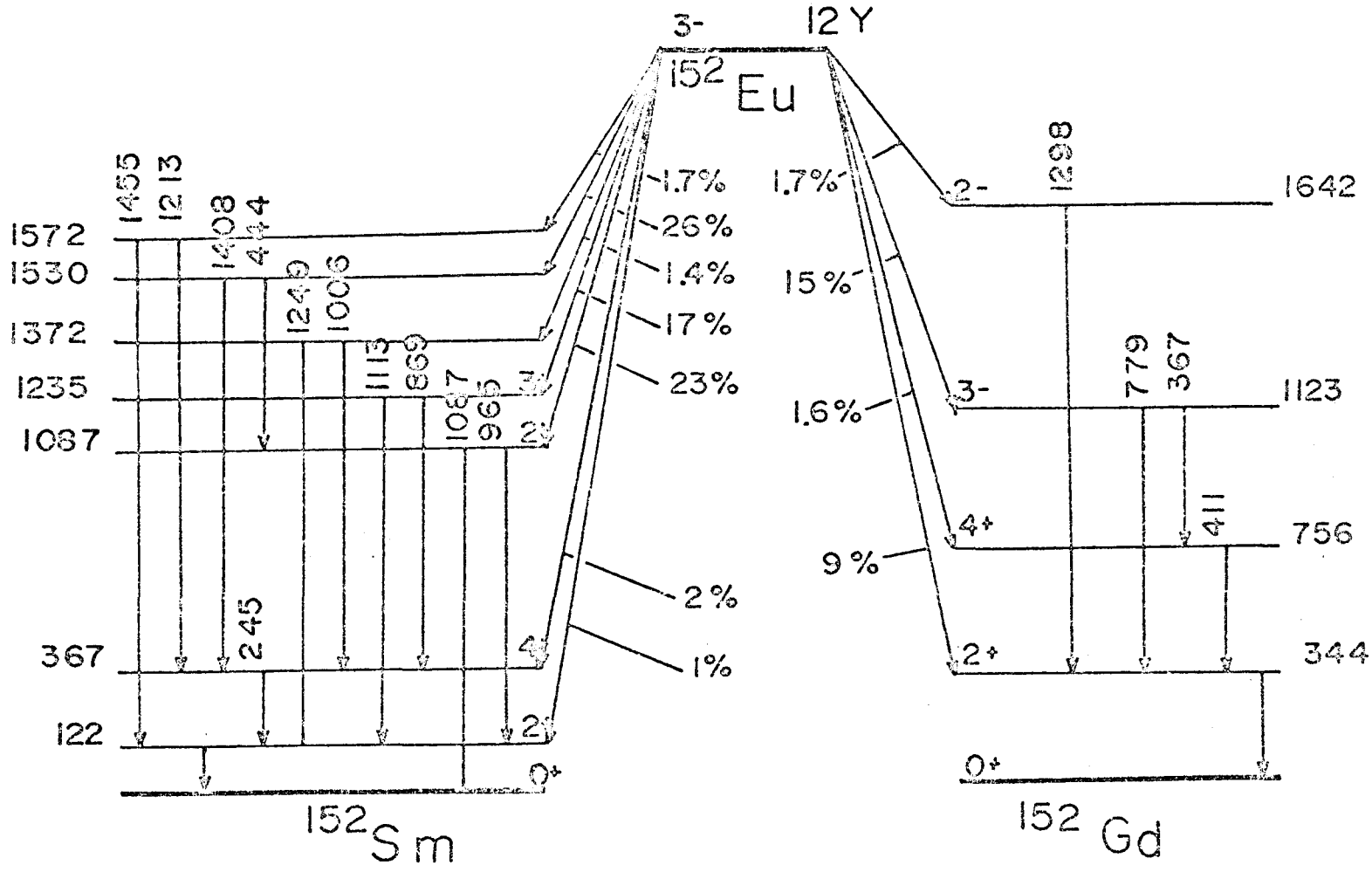
3-
12 Y
152 Eu
1455
1213
1408
444
1249
1006
1113
869
1087
965
245
1572
1530
1372
1235
1087
367
122
0+
2
4
2
2
1.7%
26%
1.4%
17%
23%
2%
1%
1.7%
15%
1.6%
9%
2-
1298
1642
3-
779
367
1123
4+
411
756
2+
344
0+
152 Sm
152 Gd

Fig. IV-2. Spectrum of ^{152}Eu (12 years half life) obtained with NaI(Tl) detector.

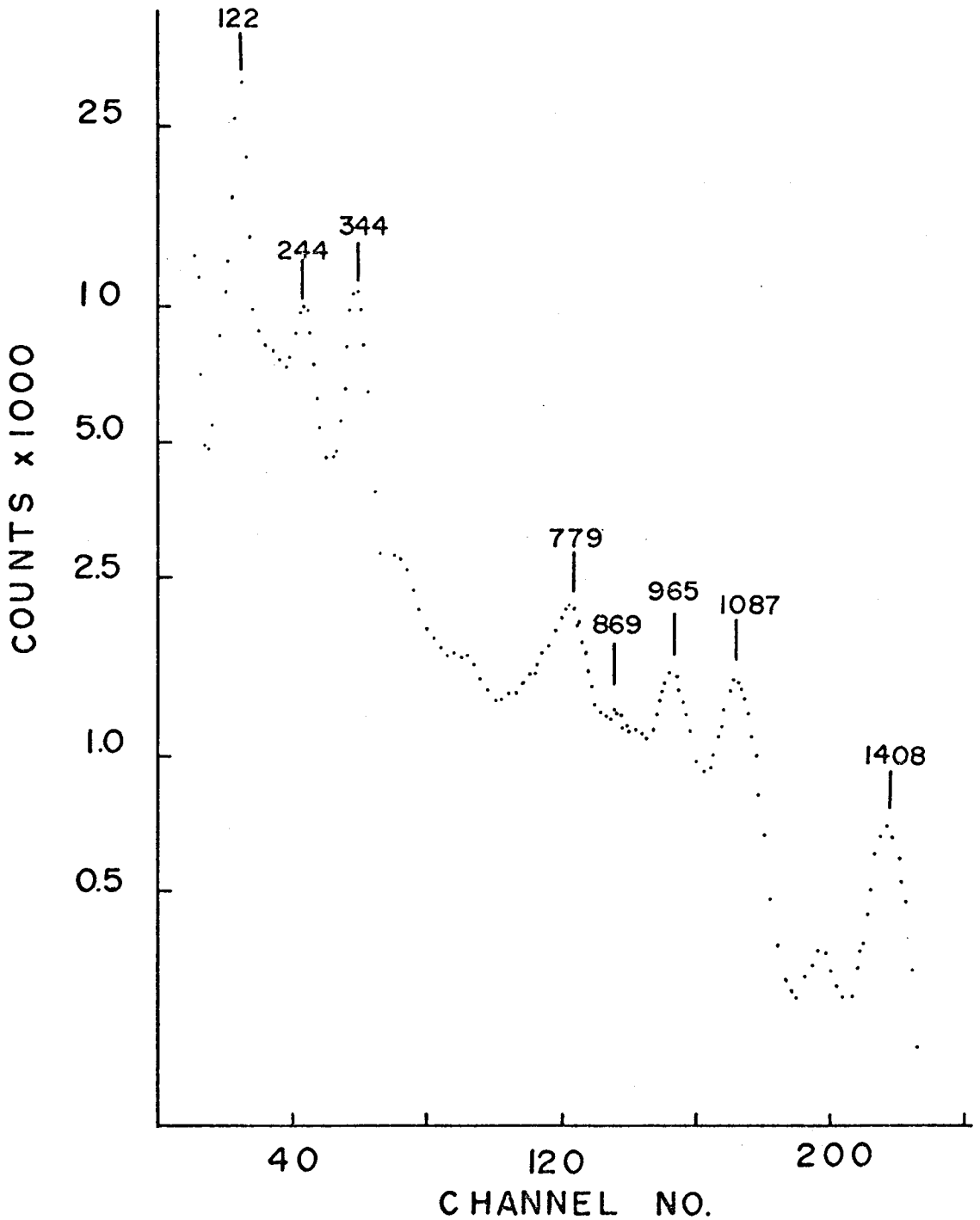
122
344
244
779
965
869
1087
1408
25
10
5.0
2.5
1.0
0.5
COUNTS x 1000
40
120
200
CHANNEL NO.

on another detector's energy spectrum. The coincidence spectra are denoted by the same letter used to label the energy window on the complete ^{152}Eu spectrum. In both Figure IV-3 and Figure IV-4 the ^{152}Eu spectrum has the last 100 channels and first 20 channels deleted resulting in a different appearance from the ^{152}Eu spectrum in Figure IV-2.

The prominence of the 779 keV peak and the 344 keV peak in the coincidence spectra A and B (Figure IV-3) indicate that there is little interference due to other cascades during the angular correlation and perturbed angular correlation measurements. In Figure IV-4 the 868 keV peak is weak in the coincidence spectrum C but the 244 keV peak is very prominently displayed in the coincidence spectrum D. Thus the only possible interference in this cascade can be effectively removed by the TSCA's. Therefore, no interference is expected in the measurement of the directional and perturbed directional correlation.

2. Sources

Alloys of europium as low concentration impurities (1 - 2%) in gadolinium, holmium, dysprosium and terbium were obtained from Research Chemicals Incorporated. These alloys were produced in induction furnaces under several atmospheres pressure of argon and rapidly cooled so they resembled castings. The sources were then prepared by cutting a 3 mm. by 1 mm. size sample from each alloy and then activated by neutron capture in the McMaster reactor.

Fig. IV-3. Coincidence spectra ^{152}Gd side. The windows A and B are marked on the ^{152}Eu spectrum. The spectra labelled A x 10 and B x 10 are the spectra in coincidence with the windows labelled A and B respectively with the counts per channel multiplied by 10.

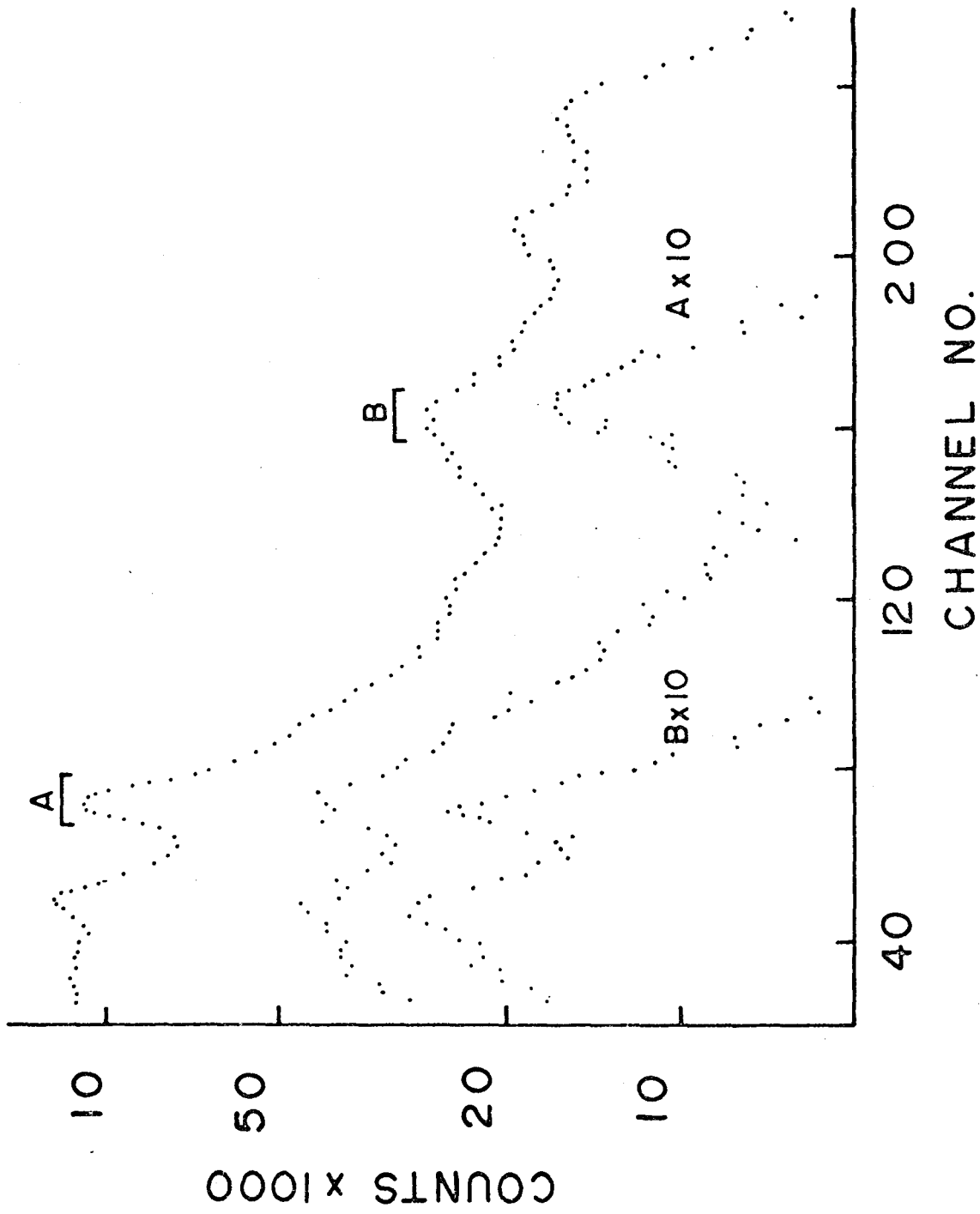
A
B
A x 10
B x 10
40
120
200
CHANNEL NO.
10
50
20
10
COUNTS x 1000

Fig. IV-4. Coincidence spectra ^{152}Sm side. The windows C and D are indicated on a ^{152}Eu spectrum. The spectra labelled C x 10 and D x 20 are the spectra coincidence with windows C and D respectively multiplied by 10 and 20 respectively.

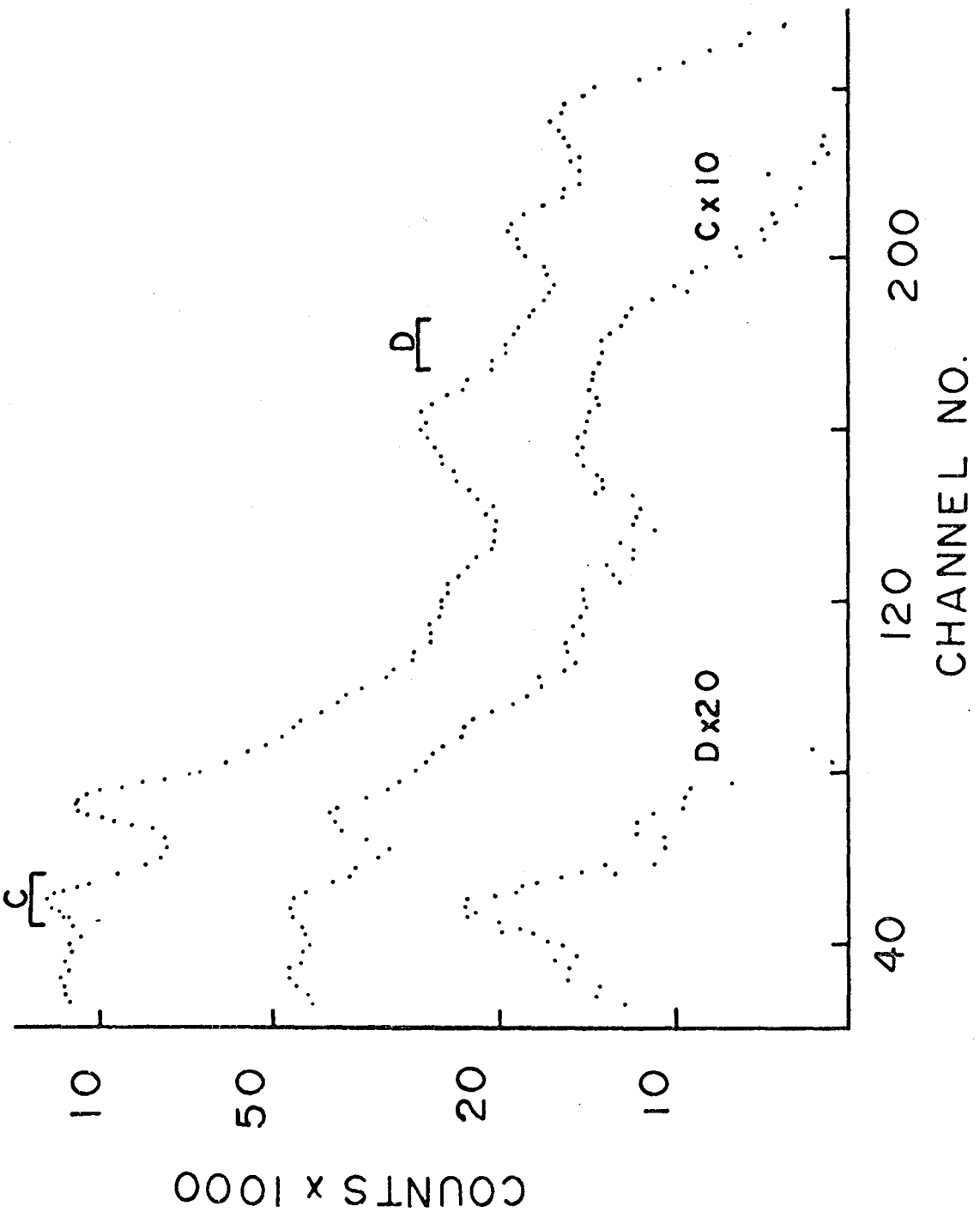
C
D
C x 10
D x 20
40
120
200
CHANNEL NO.
10
50
20
10
COUNTS x 1000

The sources were allowed to decay for a month or more so that only the 12.4 year half life ^{152}Eu was prominent in the gamma spectrum.

3. Measurement of the Unperturbed Angular Correlation

Measurement of the directional correlation of both the 868 - 244 keV ^{152}Sm cascade and the 779 - 344 keV ^{152}Gd cascade were made using the windows indicated in Figure IV-3 and Figure IV-4. This directional correlation was performed using the automated angular correlation table, employing the two moveable detectors mounted at 90° to each other and the coincidence rates were measured every $22\frac{1}{2}°$ from 90° to 180° with respect to the fixed detector.

The coincidence rates were corrected for variations in singles rates (i.e. changes in source to detector distances) for variations in the chance rate and for decay. This data was then least squares fitted to give the coefficients b_n in the expansion

$$W(\theta) = b_o + b_2 \cos 2\theta + b_4 \cos 4\theta$$

normalizing to $b_o = 1$.

For the

^{152}Sm 868 - 244 keV cascade

$$W(\theta) = 1.000 - (0.2096 \pm .0043) \cos 2\theta + (0.0317 \pm .0046) \cos 4\theta$$

For the

^{152}Gd 779 - 344 keV cascade

$$W(\theta) = 1.000 - (0.0458 \pm .0031) \cos 2\theta + (6.0057 \pm .0033) \cos 4\theta$$

The quoted errors are probable errors from the least squares fit. The angular distributions obtained are given in Figure IV-5 and Figure IV-6.

The theoretical values for b_2 and b_4 are calculated using the equations

$$b_2 = \frac{\frac{3}{4} A_{22}' + \frac{5}{16} A_{44}'}{1 + \frac{1}{4} A_{22}' + \frac{6}{64} A_{44}'}$$

and

$$b_4 = \frac{\frac{35}{64} A_{44}'}{1 + \frac{1}{4} A_{22}' + \frac{9}{64} A_{44}'}$$

Where A_{22}' and A_{44}' are the theoretical coefficients of the Legendre polynomials of the directional distribution corrected for solid angle via factors Q_2 and Q_4 (Yates).

$$A_{22}' = Q_2 A_{22}$$

$$A_{44}' = Q_4 A_{44}$$

where

$$A_{22} = A_2(1) A_2(2)$$

and

$$A_{44} = A_4(1) A_4(2)$$

$A_k(1)$ and $A_k(2)$ depend only on the spins and multipolarities of the first and second transition of the cascade respectively. If the first transition proceeds from I_1' to I with a mixture of multipolarities L_1 and $L_1' = L_1 + 1$ (mixing ratio δ_1) we get for $A_k(1)$

Fig. IV-5. Angular correlation function for ^{152}Eu using the windows A and B of Fig. IV-3.

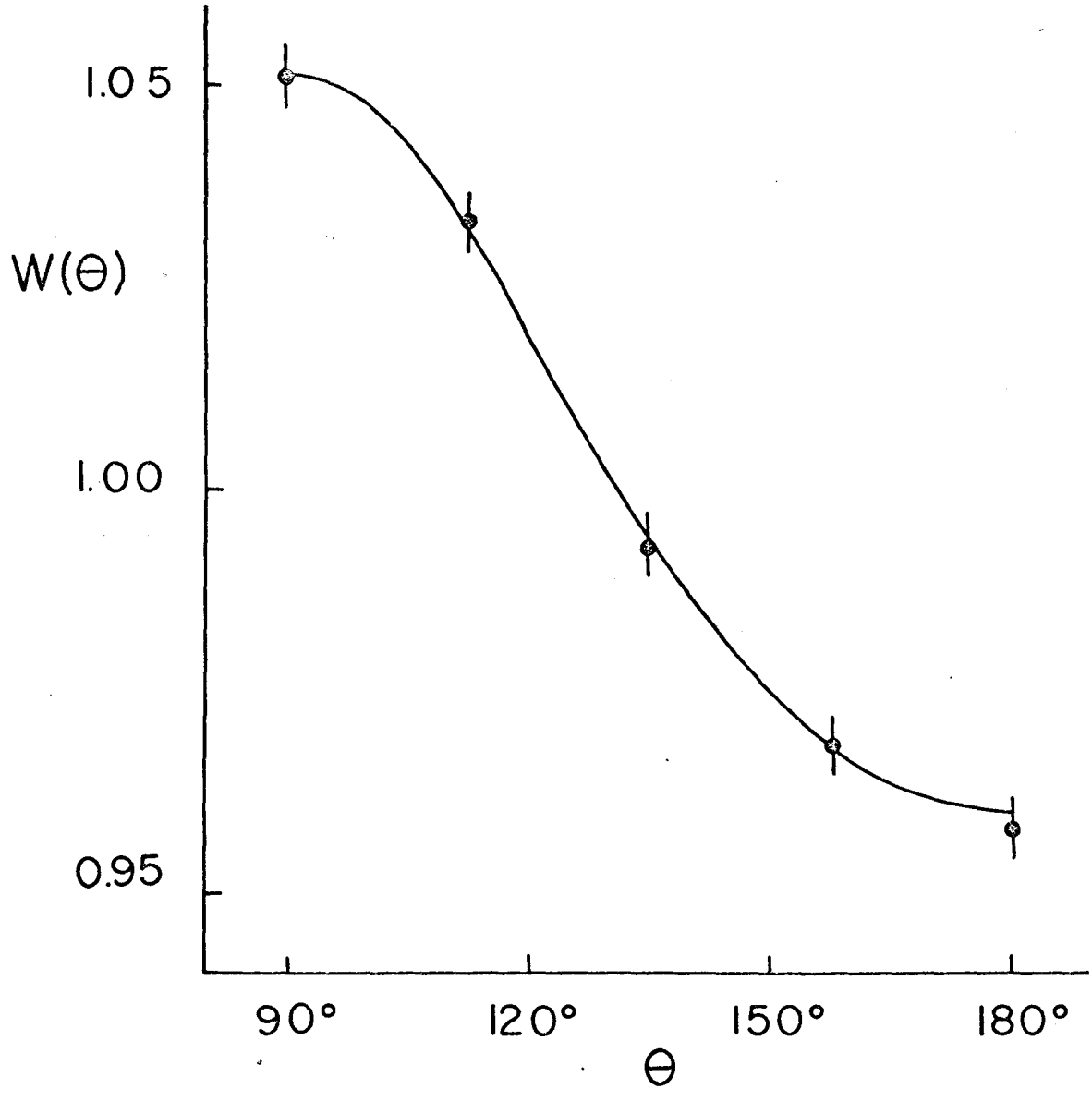
1.05
W(θ)
1.00
0.95
90°
120°
150°
180°
θ

Fig. IV-6. Angular correlation function for ^{152}Eu using the windows C and D of Fig. IV-4.

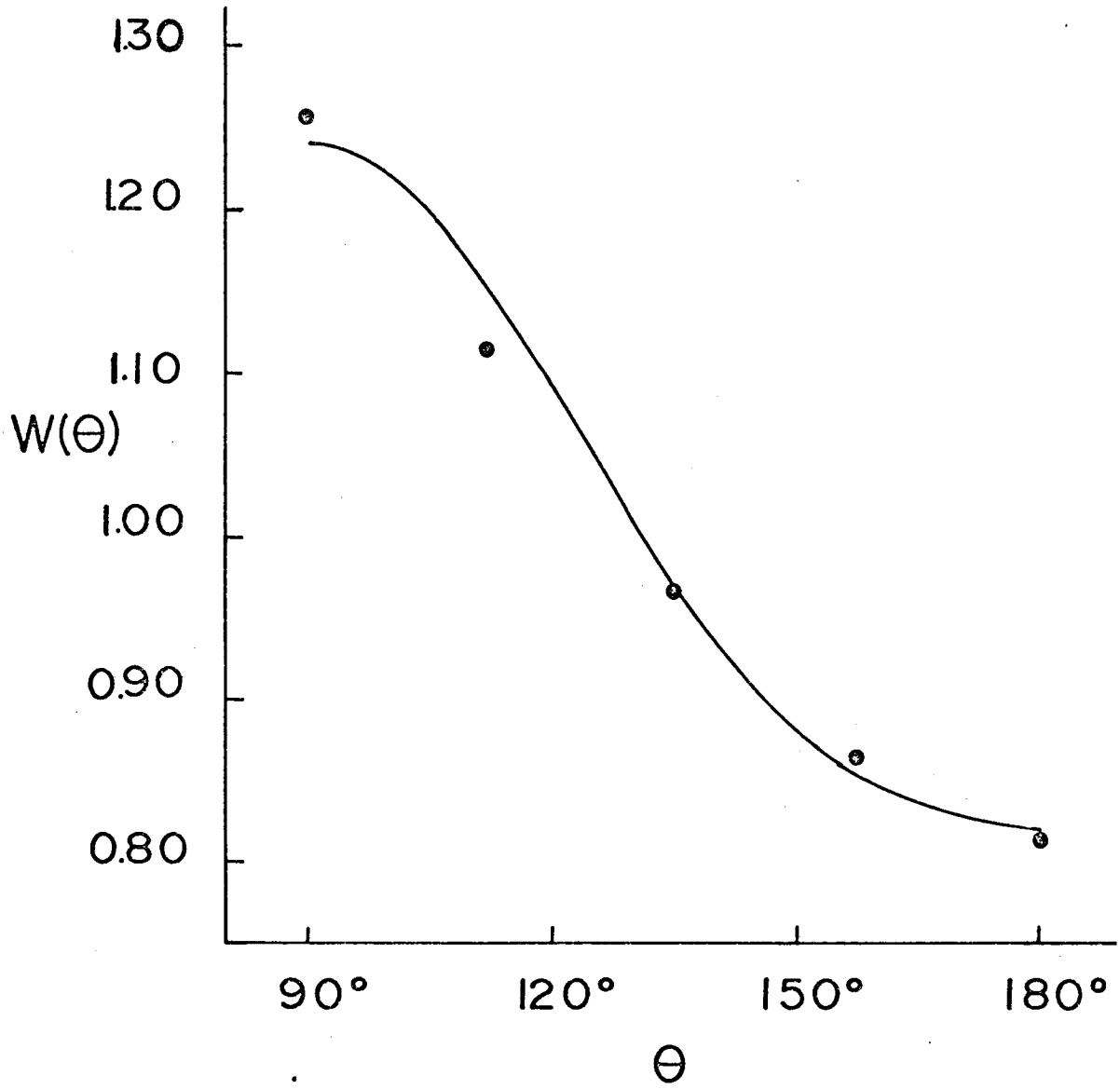
1.30
1.20
1.10
W(θ)
1.00
0.90
0.80
90°
120°
150°
180°
θ

$$A_k(1) = \frac{F_k\,(II_1'L_1L_1) + 2\delta_1 F_k\,(II_1'L_1L_1') + \delta_1^2 F_k(II'L_1'L_1')}{1+\delta_1^2}$$

and similarly for the second transition $I \rightarrow I_2'$ and L_2 mixed with $L_2' = L_2 + 1$ (mixing ratio δ_2) for $A_k(2)$

$$A_k(2) = \frac{F_k\,(II_2'L_2L_2) + 2\delta_2 F_k\,(II_2'L_2L_2') + \delta_2^2 F_k\,(II_2'L_2'L_2')}{1+\delta_2^2}$$

The F_k's are tabulated functions (Ferentz and Rosenweig).

For the ^{152}Sm 869 - 244 γ- γ cascade using the sequence 3+(1,2) 4+(2) 2+ where $\delta = 6$ (Zganjar et al 1968), one obtains

$$b_2 = -0.162$$

$$b_4 = 0.0258$$

b_2 theoretical is noticeably smaller than b_2 experimental $=-0.2096 \pm 0.0043$. This discrepancy could be removed if δ was slightly smaller as the A_{22} values are very sensitive to δ (for $\delta = 5$, $b_2 = .35$).

For the 779 - 344 γ- γ cascade in ^{152}Gd using the sequence 3-(1) 2+(2) 0+ the theoretical value of A_{22} is -0.071 (Nasir et al, 1967) which gives $b_2 = 0.0486$ which agrees within statistics with the experimental value $b_2 = 0.0458 \pm 0.0031$. The observed value for b_2 would be expected to be slightly lower than the theoretical one due to scattering from the magnetic shielding increasing the effective solid angle. There is disagreement between b_4 theoretical = 0 and $b_4$exp = 0.0057 ± 0.0033, but this

variation is acceptable being within two statistical deviations.

4. Measurement of the Rotations

The rotation of the 366 keV level of ^{152}Sm alloyed into Gd was measured once at liquid nitrogen temperatures using the iron magnet and the liquid nitrogen dewar. Similarly the rotation of the ^{152}Gd 344 keV level was measured twice using the same setup. The sample was tested for magnetic saturation using standard techniques in which a signal is produced whose amplitude is proportional to the magnetization. The signal amplitude curve is shown in Figure IV-7 was obtained. The magnet was operated at 1.25 amps well beyond the knee of the saturation curve. These runs produced the following results:

Isotope	$\frac{R}{2}$	$\omega\tau$ in radians
^{152}Sm	$< 1.3 \times 10^{-4}$	$< 2.4 \times 10^{-4}$
^{152}Gd	$2.21 \pm 0.46 \times 10^{-3}$	$2.39 \pm 0.51 \times 10^{-2}$

Subsequently an experiment was performed on ^{152}Eu, in the europium - holmium alloy, at 4.2° K. Since the sample employed was extremely small no magnetic saturation tests were performed. The magnet was operated at 15 amps corresponding to a field of 13.2 kilogauss which was assumed to be sufficient for magnetic saturation of holmium. The detectors were positioned 10 cm. from the source at 135° with respect to the "fixed" detector. The following

Fig. IV-7. Magnetic saturation curve for europium - gadolinium alloy.

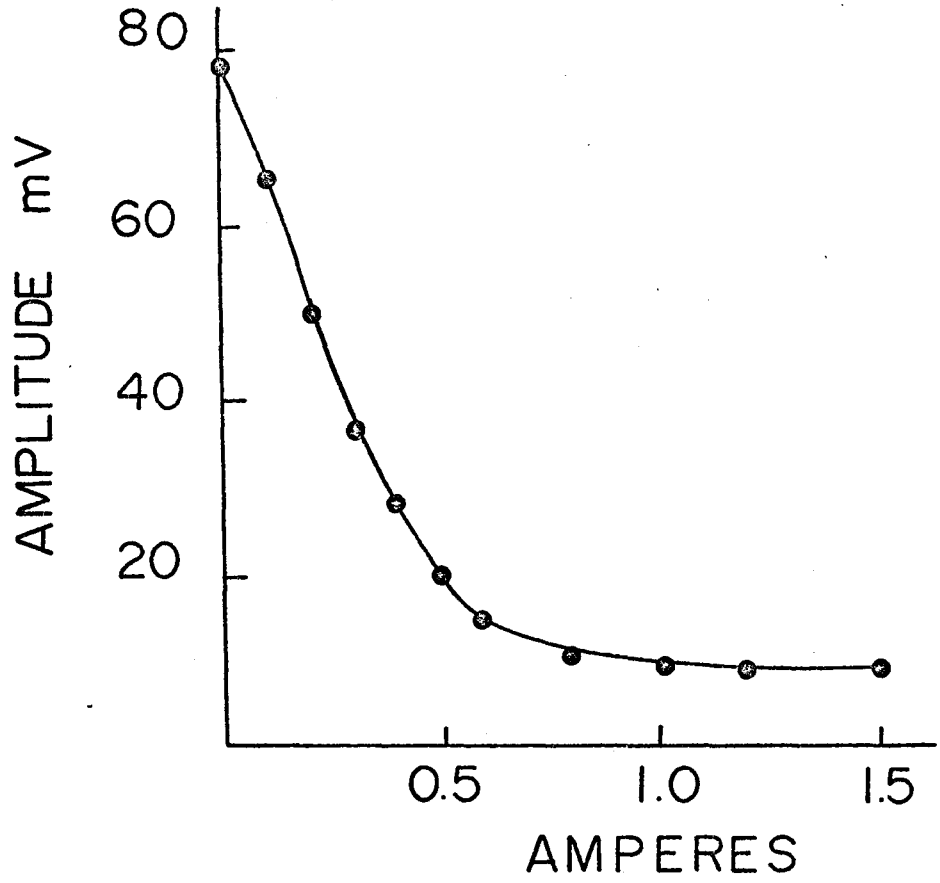
80
60
40
20
AMPLITUDE mV
0.5
1.0
1.5
AMPERES

results were obtained

Isotope	$\frac{R}{2}$	$\omega\tau$ in radians
^{152}Sm	$< 1.6 \times 10^{-3}$	$< 3.6 \times 10^{-3}$
^{152}Gd	$9.46 \pm 4.82 \times 10^{-4}$	$1.03 \pm 0.54 \times 10^{-2}$

An experiment to determine the g-factor of the 2+ level in ^{152}Gd had been performed previously using both the 779 - 344 keV cascade and the 1298 - 344 keV cascade for ^{152}Gd in Gd by Zamora et al (1969). Zamora obtained a value for $2\omega\tau$ of 0.074 ± 0.0067 for the 779 - 344 keV cascade with the source maintained at 85° K and $H_{eff} = -320 \pm 15$ kOe. Thus there is a noticeable discrepancy in the value of $\omega\tau$ obtained by Zamora and the results obtained for ^{152}Gd in Gd in the results recorded above.

5. Etching of Samples

As a result of the discrepancy between the rotation obtained by Zamora et al, for the 344 level of Gd in Gd and the experimental results recorded above it was decided to reinvestigate the homogeneity of the alloys. Prior to the experiments being performed the samples had been scanned with the electron microprobe and appeared homogeneous.

The initial polishing of the alloys was done in water using successively finer grain emery paper in four steps from 220 to 600. Each polishing took about five minutes. None of the alloys showed signs of corrosion under the 800 power microscope after polishing on the emery paper and a methanol wash.

The samples were then polished for three minutes on 25 micron alumina powder polishing boards with a kerosive medium. The samples were then washed with methanol.

The samples were then polished on low speed wheels with a microcloth impregnated with a 6 micron diamond paste using a kerosene media. After another methanol wash the sample was polished with a 1 micron diamond paste again using a kerosene media. Each of these polishing steps took five to ten minutes. The sample was washed after this final polishing with methanol and air dried. As there were no scratches observable this polishing appeared sufficient for observation purposes. However, some people make use of finer abrasives such as 0.3 micron alumina or 0.25 micron diamond.

Before etching began on any sample microscopic examination was performed at 800 power to examine the effects of polishing.

The samples were etched by a 10% nital solution (i.e. 10% solutions of nitric acid in ethyl alcohol), for a period of about ten minutes after which the surface was flooded with methanol to remove any remaining nital and quench the etch. Nital appeared satisfactory for these investigations although some prefer to make use of a non aqueous phosphoric acid etchant for rare earth alloy systems (Spedding and Daane, 1961).

The initial europium (1%) in gadolinium alloy was

observed under an 800 power microscope to have a grain size of about 3 microns by 10 microns. There were small areas (inclusions) less than 0.8 microns in size present throughout the sample as shown in Figure IV-7. The grains all possess a rectangular shape and the long axis of the rectangles is roughly parallel to the long axes of the neighbouring grains. If this tendency of grain shape towards alignment is indicative of the crystal axes then the samples would not consist of randomly oriented grains.

Part of the europium (1%) in gadolinium alloy was annealled at 1050° C for 48 hours in a vacuum. After etching it showed a grain size of approximately 2 mm. and the inclusions had grown to about 10 microns in size.

Both of these samples were re-examined using the electron microprobe and the results are shown in Figure IV-9 and Figure IV-10. Basically the electron microprobe focuses an electron beam, approximately 1 micron in diameter onto the sample under investigation, thereby producing the X-ray spectra characteristic of the elements constituting the sample. Via crystal diffraction techniques the X-rays corresponding to an arbitrary wavelength are allowed to impinge upon the NaI(Tl) detector, which produces a signal whose amplitude is proportional to the number of X-rays striking it. The diffracting crystal can be oriented so that the K X-rays of only the desired element reach the detectors. In this manner the variation of concentration

Fig. IV-8. Typical etched alloy sample.

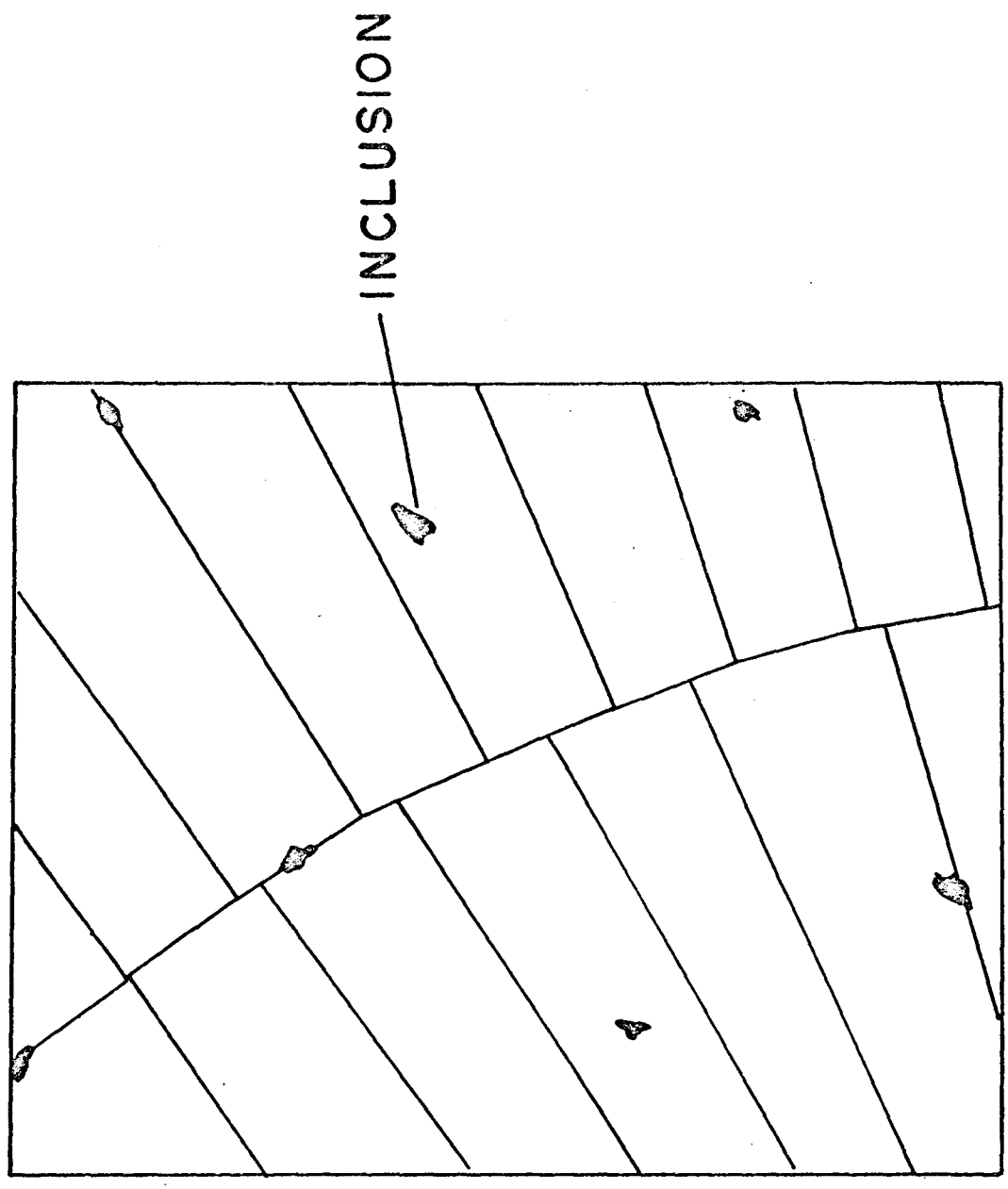
INCLUSION

of an element over a region can be observed. In the actual apparatus there are two sets of detectors and crystals enabling the X-rays of two different elements to be observed simultaneously.

The beam of electrons from the microprobe was moved across the sample until it was aimed on the inclusion and then was moved off the inclusion and across the sample to where there were no visible inclusions. The amplitudes of the signals were simultaneously recorded using a chart recorder. Figures IV-9 and Figure IV-10 represent the smoothed signal output. In Figure IV-9 the signal for europium grew to about 10 times the strength for the background when it was placed on the inclusion while the signal for gadolinium decreased by about 10%. Since the electron probe spot is about twice as large as the inclusion and there are problems in aiming the probe accurately, all that can be determined is that the inclusion is an area of very high europium concentration.

The electron microprobe results for the annealled sample showed that the inclusions in it were virtually all europium with little or no gadolinium present.

Upon etching, the remainder of the europium - rare earth alloys: holmium, dysprosium, and terbium; appeared similar to the unannealled sample of europium in gadolinium. The only variations amongst the samples were in the size of the grains and the size of the larger inclusions present,

Fig. IV-9. Electron probe results for a sample of the europium - gadolinium alloy.

Fig. IV-10. Electron probe results for the annealled sample of the europium - gadolinium alloy.

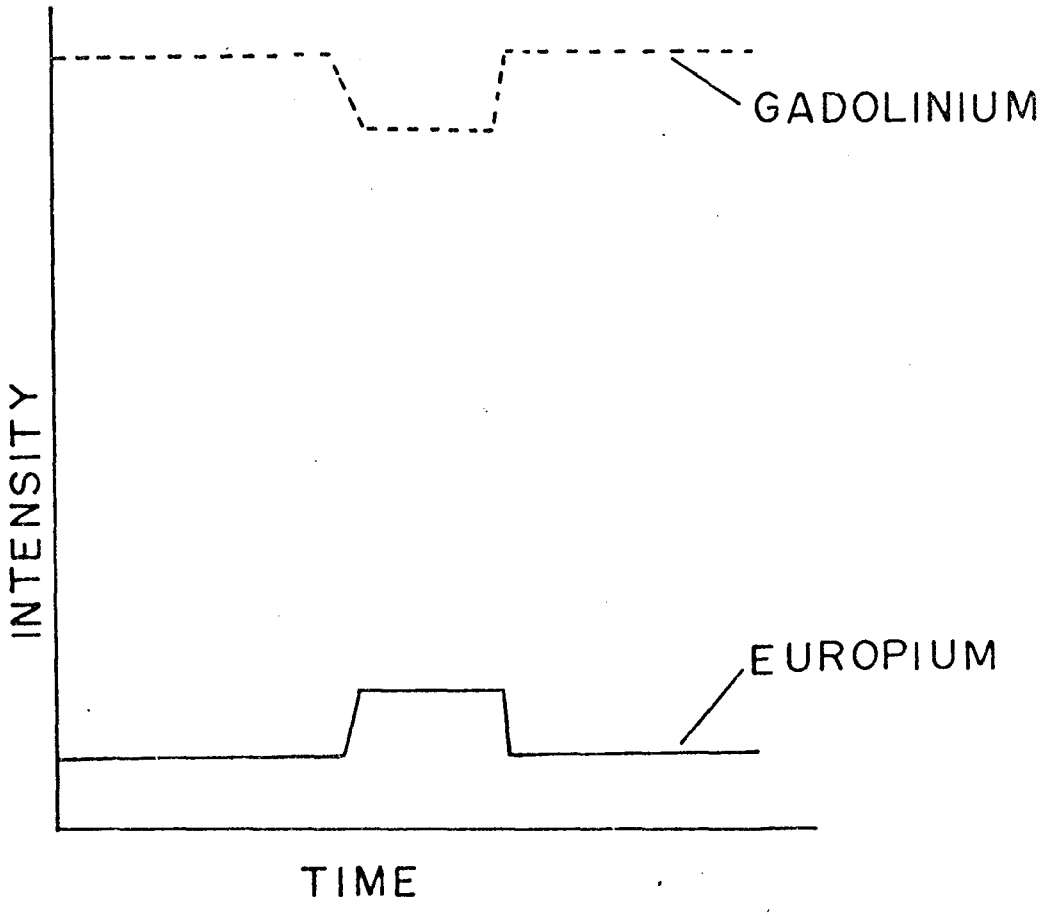
GADOLINIUM
EUROPIUM
INTENSITY
TIME

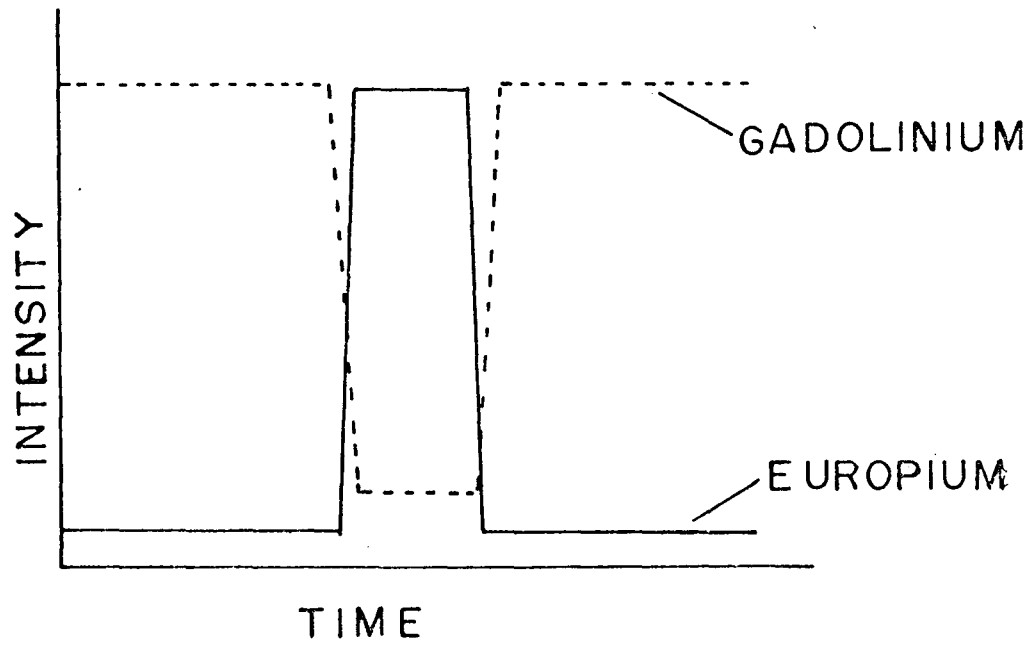
GADOLINIUM
EUROPIUM
INTENSITY
TIME

but both grain and inclusion size variations were within a factor of two.

6. Discussion

An experimental value of g = + 0.32 ± 0.06 was obtained by Zamora et al (1969) for the 344 keV level in ^{152}Gd which agrees within experimental error with the calculations of Greiner (g = 0.36) and the quasi particle model estimates (g = 0.299) Baranger et al (1968). Thus Zamora's value of g = 0.32 will be assumed for the calculation of H_{eff} acting on ^{152}Gd in Gd and in Ho. Our experimental results for Gd in Gd give H_{eff} = - 204 ± 40 kOe. based on τ = 7.6 ± 1.3 x 10^{-11} sec. where the only error is assumed to be statistical.

This compares rather unfavourably with the expected value

$$H(77K) = \frac{M}{M_s} H(0^{\circ}K) - H_{dem} - H_{ext}$$

$$= - 325 \pm 20 \text{ kOe}$$

where M and M_s are the magnetizations of gadolinium at 77° K and 0° K respectively. H_{dem} is the demagnetizing field and H_{ext} is the external magnetic field.

The discrepancy can be explained if not all of the ^{152}Gd nuclei contribute to the observed rotation. Since europium is antiferromagnetic below 91° K and the inclusions appear to be completely europium, the assumption that H_{eff} = 0 for the nuclei in the inclusions is justified. Thus it would appear that 62 ± 12% of the europium atoms are in proper gadolinium lattice sites and the remainder are in

the inclusions.

In the holmium alloy the field on the ^{152}Gd nuclei was measured to be $H_{eff} = -89 \pm 45$ KG. The exact meaning of this measurement is not obvious as the effective field on gadolinium in holmium is not known and the relative amount of europium in lattice sites is not known directly. Assuming the field is the same as for Gd in Gd the amount of europium in holmium lattice sites is $(27 \pm 13)\%$ of the europium present. Since all the inclusions are less than a micron in size a visual estimate of the amount of europium in the inclusions becomes quite difficult. Added to this, the amount of europium in the sample is known only to a factor of two and the concentration may vary from one region of the sample to another.

In the case of ^{152}Sm in gadolinium at 77° K a magnetic field $H_{eff} < 2.0$ KG acts on the samarium nuclei. The value is arrived at by using the value

$$\tau = 1.13 \pm .23 \times 10^{-11} \text{sec.}$$

for the 366 keV level and using $g \simeq 0.3$ which is a conservative value. So effectively one could consider $H_{eff} = 0$ on the samarium nucleus which might be expected as samarium is antiferromagnetic in this temperature region. For the ^{152}Sm in the holmium alloy H_{eff} is less than 21 kOe. Again H_{eff} on a samarium nucleus is close to zero as might be expected.

The cause of the inclusions is puzzling. It is known that differences in atomic size as well as differences

in electronegativity affect the alloying of two elements. The Darken - Gurney plots (Gschneider) Figure IV-11 and Figure IV-12, illustrate these two criterion simultaneously by means of ellipses. The major axis represents a given electronegativity difference and the minor axis represents a set per cent size difference and the ellipse is centred on the host element in the alloy. The small ellipse has axes of $\pm$ 0.2 electronegativity units and a $\pm$ 8 per cent size difference in atomic radii. Elements within the ellipse are expected to form homogeneous alloys with the host element. The larger ellipse has a $\pm$ 15 per cent atomic radii size difference and a $\pm$ 0.4 difference in electronegativity units and there is a limited solubility of elements in the region between the larger and smaller ellipses. Elements outside the larger ellipse have very limited or non-existant solubility with the element the ellipse is centred on. As can be seen in Figure IV-11, europium is near the boundary of the larger ellipse. This might be the source of the inclusions - a very limited solubility. However, a Lu (1%) in Gd alloy was produced by the same method as the other alloys and upon etching it also showed the presence of inclusions and as can be seen from Figure IV-11, Lu is well within the small ellipse for Gd on the Darken - Gurney plot.

Thus the problem of inclusions might be a result of the method of production of the alloys rather than any alloying criterion.

Fig. IV-11. Darken - Gurney plot for Gadolinium, Scandium, and Yttrium.

Fig. IV-12. Darken - Gurney plot for Europium and Ytterbium.

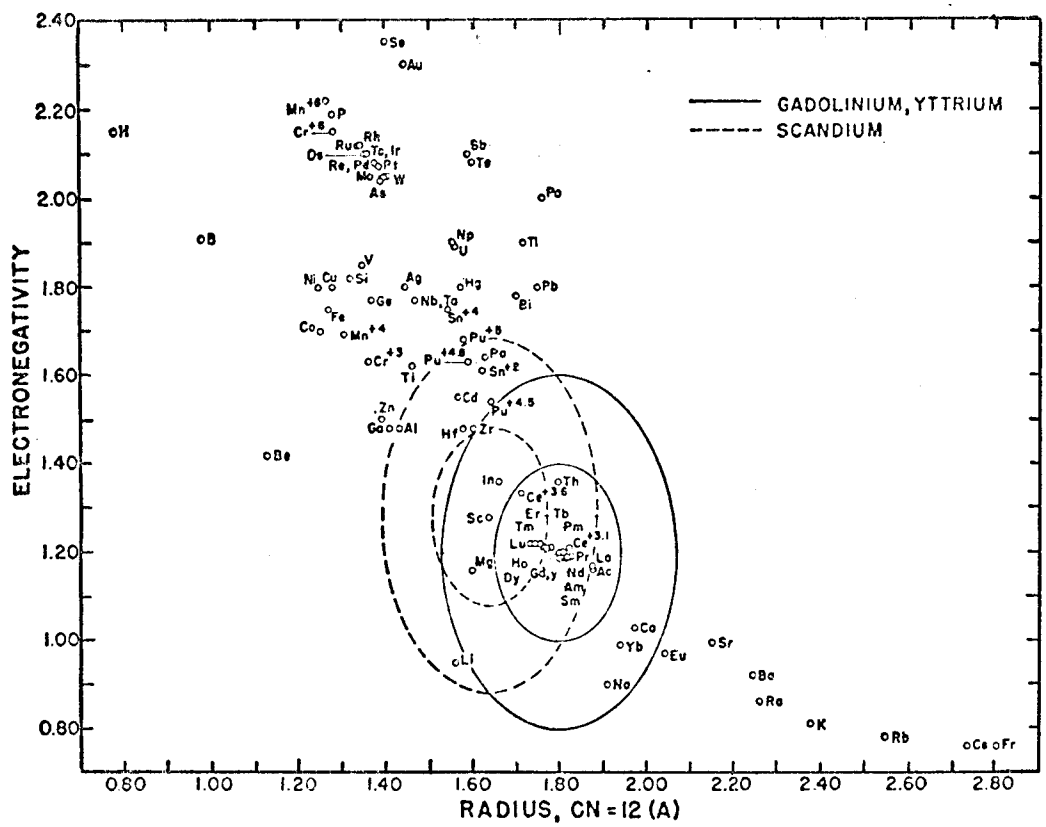
GADOLINIUM, YTTRIUM
SCANDIUM
ELECTRONEGATIVITY
RADIUS, CN = 12 (A)
2.40
2.20
2.00
1.80
1.60
1.40
1.20
1.00
0.80
0.80
1.00
1.20
1.40
1.60
1.80
2.00
2.20
2.40
2.60
2.80

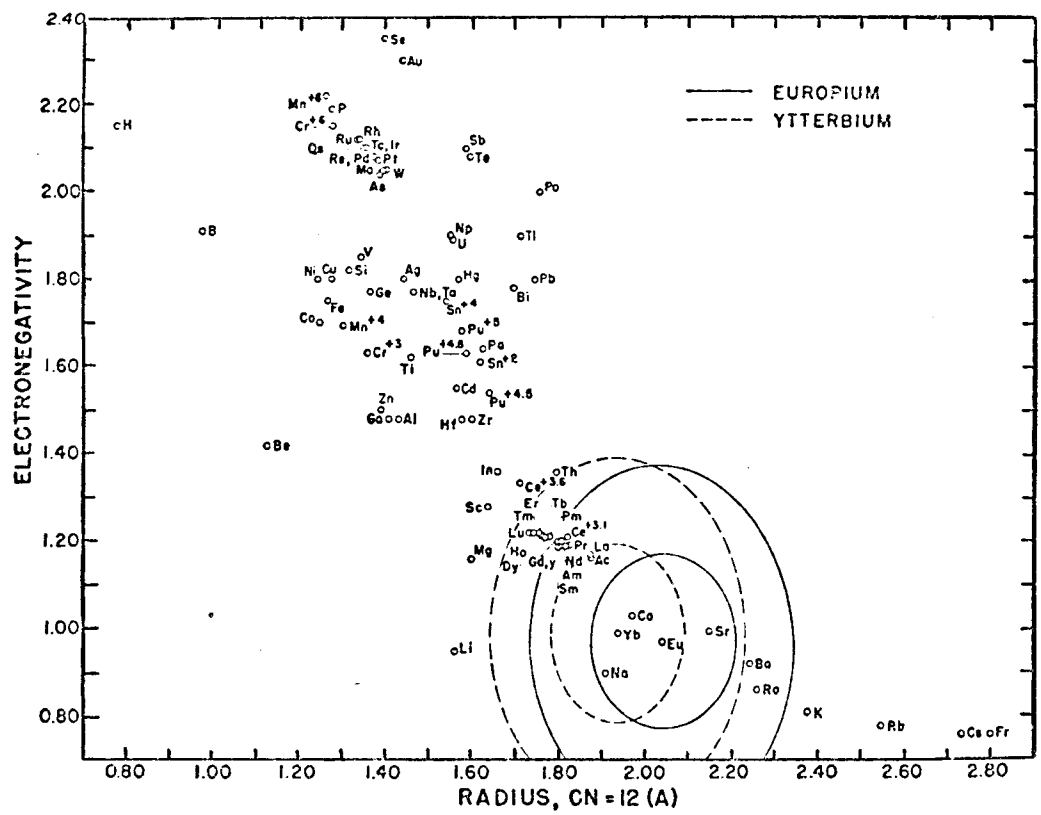
EUROPIUM
YTTERBIUM
ELECTRONEGATIVITY
RADIUS, CN = 12 (A)
2.40
2.20
2.00
1.80
1.60
1.40
1.20
1.00
0.80
0.80
1.00
1.20
1.40
1.60
1.80
2.00
2.20
2.40
2.60
2.80

The results of Zamora et al, for ^{152}Sm at 130^{o} K produced an internal field in agreement with earlier work by Murnick et al. Also, the value of the g-factor for the 344 keV level in ^{152}Gd agrees with theory. Both of these tests on H_{eff} indicate that it is possible for europium to be alloyed into gadolinium and for substantially all the europium to be at the gadolinium lattice sites.

CHAPTER V

CONCLUSIONS

The importance of proper metallurgical analysis for determining sample homogeneity is demonstrated as the initial electron probe results showed the sample to be homogeneous. The later analysis, after etching, confirmed the doubts raised by the perturbed angular correlation results as to the sample being a true alloy since inclusions were present. Also, the etched samples indicated that the crystallites were not randomly oriented although the grain size meant there would be about 10^4 to 10^6 grains in a typical source sample. This non-random orientation can be critical with the rare earth metals due to the presence of the hard direction of magnetization present in most elements which become ferromagnetic. Hence where a single crystal cannot be obtained it would be better to transform the alloy sample from a rod into a fine powder or shavings, so that the source possesses the desired random orientation of the crystallites. The problem of the non-random crystal orientation in the holmium alloy might be contributing to the lowering of H_{eff} as holmium has a hard C axis for magnetization.

In cases where the g-factor of a nuclear level is known and the hyperfine magnetic field is also known for

the alloy under investigation, the technique of perturbed angular correlations can be employed as a check of the percentage of the impurity which is in solid solution with the host material. This can be valuable as the inclusions can be present but not readily visible by metallurgical techniques as was the case for the europium (1%) in gadolinium alloy. Also, the method can provide a quantitative analysis of the amount of impurity not in solution. Again, referring to the europium - gadolinium alloy the results indicated that $40 \pm 10\%$ of the europium was in the inclusions.

The results, both metallurgical as well as nuclear investigations indicate that there is a great difficulty in alloying small (1 - 2%) amounts of an impurity rare earth into a rare earth host material. Since the sources - all five (Lu - Gd, Eu - Gd, Eu - Ho, Eu - Tb, and Eu - Dy) - were commercially obtained from the same firm and showed the same problems with inclusions, the fault probably lies in the method of production employed.

Since H_{eff} acting on a samarium nucleus, where no averaging over orientations occurs, is approximately 3,000 kilogauss from specific heat data an estimate of the number of aligned samarium nuclei can be made. In the case of the gadolinium host less than 0.05% of the samarium nuclei were aligned along the external magnetic field direction. Similarly in the case of the holmium less than 0.1% of the samarium nuclei were aligned with respect to the external field.

REFERENCES

Alkhazov, D.G., Vasil'ev, V.D., and Grangrshii, Yu.P. 1964. Bulletin Acad. Sci. USSR. 28 - 146.

Behrendt, D.R., Legvold, S., and Spedding, F.H. 1958. Phys. Rev. 109 - 1544.

Burde, J., Rakay, M., and Ofer, S. 1961. Phys. Rev. 124 - 1911.

Ferentz, M., and Rosenzweig, N. 1965. Alpha-, Beta-, Gamma-Ray Spectroscopy Appendix 8 (North Holland, Amsterdam - edited by K. Seigbahn.

Freeman, A.J., and Watson, R.E. 1961. Phys. Rev. 123 - 2027.

Greiner, R. 1965. Nuc. Phys. 80 - 417.

Gschneider, K.A. 1961. Rare Earth Alloys (Van Nostrand, Toronto).

Kasuya, T. 1956. Prog. Theo. Phys. 16 - 45.

Koehler, W.C. 1965. Jour. App. Phys. 36 - 1078.

Kondo, J. 1961. J. P. Soc. Jap. 16 - 1690.

Kumar, K., and Baranger, M. 1968. Nuc. Phys. A 110 - 529.

Lederer, C.M., Hollander, J.M., and Perlman, I. 1968. Table of Isotopes Sixth Edition (John Wiley and Sons, New York).

Marshall, W. 1958. Phys. Rev. 110 - 1280.

Kurnick, D.E., Grodzens, L., Bronson, J.D., Herskind, B., and Borchers, R.R. 1967. Phys. Rev. 163 - 254.

Nasir, H., Gabrowski, Z.W., Steffen, R.R. 1967. Phys. Rev. 162 - 1118.

Rado, G.T., and Suhl, H. 1965. Magnetism Vol. II A (Academic Press, New York).

Rudderman, M.A., and Kittel, C. 1954. Phys. Rev. 96 - 99.

Spedding, F.H., and Daane, A.H. 1961. Rare Earth Metals (John Wiley and Sons, New York).

Steffen, R.M., and Frauenfelder, H. 1965. Alpha-, Beta-, Gamma-Ray Spectroscopy pp. 997-1198 (North Holland, Amsterdam - edited by K. Seigbahn).

Yates, M.J.L. 1965. Alpha-, Beta-, Gamma-Ray Spectroscopy Appendix 9 (North Holland, Amsterdam - edited by K. Seigbahn).

Yosida, K. 1957. Phys. Rev. 106 - 893.

Yosida, K. 1964. Progress in Low Temperature Physics pp. 265-295 (North Holland, Amsterdam - edited by Gorten).

Zamora, H., Blau, M., and Ofer, S. 1969. Nuc. Phys. A 130 - 541.

Zganjar, E.F., George, T.M., and Hamilton, J.H. 1968. Nuc. Phys. A 114 - 609.